This is the peer reviewed version of the following article: Phys. Status Solidi A 209, No. 1, 181–192 (2012), which has been published in final form at https://onlinelibrary.wiley.com/doi/full/10.1002/pssa.201127595 . This article may be used for non-commercial purposes in accordance with Wiley Terms and Conditions for Use of Self-Archived Versions.

Mechanism of Surface Proton Transfer Doping in Pentacene based Organic Thin-Film Transistors

By *Simon J. Ausserlechner*, *Manfred Gruber*, *Reinhold Hetzel*, *Heinz-Georg Flesch*, *Lukas Ladinig*, *Lucas Hauser*, *Anja Haase*, *Michael Buchner, Roland Resel, Ferdinand Schürrer, Barbara Stadlober, Gregor Trimmel*, *Karin Zojer* and *Egbert Zojer**

[*] Prof. E. Zojer, S. J. Ausserlechner, R. Hetzel, Dr. H.-G. Flesch, L. Ladinig, Prof. Roland Resel

Institute of Solid State Physics, Graz University of Technology

Petersgasse 16, 8010 Graz (Austria)

E-mail: egbert.zojer@tugraz.at

M. Gruber, M. Buchner, Prof. F. Schürrer, Dr. K. Zojer

Institute of Theoretical and Computational Physics, Graz University of Technology

Petersgasse 16, 8010 Graz (Austria)

L. Hauser, Prof. G. Trimmel

Institute for Chemistry and Technology of Materials, Graz University of Technology

Stremayrgasse 9, 8010 Graz (Austria)

Dr. A. Haase, Dr. B. Stadlober

Institute of Nanostructured Materials and Photonics, Joanneum Research

Franz-Pichler-Straße 30, 8160 Weiz (Austria)

Keywords: Organic Thin-Film Transistor, Pentacene, Threshold Voltage, Surface Proton Transfer Doping, Space Charge Layer, Device Modelling

A number of studies show that chemical modification of the semiconductor-dielectric interface can be used to control the threshold voltage (V_{th}) of organic thin film transistors (OTFTs). A promising chemical functionality to achieve that are acidic groups, which - at the semiconductor-dielectric interface - have been used to realize chemically responsive OTFTs and easy to fabricate inverter structures. Especially for pentacene-based OTFTs, the underlying chemical and physical mechanisms behind the acid-induced V_{th} shifts are not yet fully understood. Their clarification is the topic of the present paper.

To distinguish between space-charge and dipole-induced effects, we study the impact of the thickness of the gate oxide on the device characteristics achieving maximum V_{th}-shifts around 100 V. To elucidate the role of the acid, we compare the doping of pentacene by acidic interfacial layers with the impact of hydrochloric acid vapour and investigate the consequences of exposing devices to ammonia. Complementary experiments using 6,13-bis(triisopropylsilylethynyl)pentacene as active layer hint towards the central (6 and 13) carbon atoms being subject to the electrophilic attack by the acidic protons. They also prove that the observed V_{th} shifts in pentacene devices are indeed a consequence of the interaction between the acidic groups and the active material. The experimental device characterization is supported by drift-diffusion based device modelling, by quantum chemically simulations, as well as by contact angle, atomic force microscopy, x-ray reflectivity, and x-ray diffraction measurements. The combination of the obtained results leads us to suggest proton transfer doping at the semiconductor-dielectric interface as the process responsible for the observed shift of V_{th}.

1. Introduction

The crucial role played by the semiconductor-dielectric interface has been demonstrated by a number of studies during the past few years.[1,2] It, for example, influences charge-carrier trapping[3] and thin film growth.[4] This, in turn, determines device parameters like the carrier mobility (μ)[5-7] and the threshold voltage (V_{th}). From an application-oriented point of view, the control of V_{th} is necessary to realize low voltage operation organic electronics,[8,9] or to fabricate depletion-load inverters using only a single-type of semiconductor material.[10,11] Beyond that, understanding processes affecting V_{th} is also of fundamental interest for understanding the operation mechanism of OTFTs.

The methods developed over the years to tune V_{th} via interface modifications include: UV[10], UV-ozone,[12,13] or oxygen plasma[13] treatment of the surface of the dielectric, changing the dielectric capacitance,[14] inserting dipole-polarized[15] or polarizable layers,[16,17] or storing charges at the dielectric-semiconductor interface.[18] Of particular relevance for the present study is the use of functional self-assembled monolayers (SAMs).[19-23] Their insertion between the gate dielectric and the organic semiconductor layer has been shown to give rise to V_{th} shifts of several ten volts. A number of underlying mechanisms for the shifts have been suggested. One is the formation of dipole layers when using polar SAMs that shift the potential of the semiconductor-dielectric interface,[19-21,23] where the charge carrier transport takes place.[24] The experimentally observed V_{th} shifts did, however, not necessarily match the expectations based on the 'dipole' model.[19,22] Moreover, it was argued on the basis of a comparison between device characteristics and secondary electron emission spectroscopy experiments[7] that realistic molecular dipole moments would lead to V_{th} shifts of only a few volts. This notion has been supported by drift-diffusion based simulation.[25]

Thus, a charge transfer between the organic semiconductor and the SAM has been suggested as an alternative explanation.[19,22] This process is reminiscent of 'electronic' surface transfer doping,[26-30] where the underlying chemically process is a redox reaction between the semiconductor and the SAM.[26] The model is based on the assumption that semiconductor-dielectric interfacial space charges can shift the flat band voltage (V_{fb}) and, therefore, V_{th}. This can be derived analytically[31,32] or by numerical, drift-diffusion based simulations [25,33-35] and has also been measured in OTFTs.[18]

An analogous model has been proposed for OTFTs containing acidic SAMs using regioregular poly(3-hexyl-thiophene) (rr-P3HT) as the active layer. In such devices, the "normally on" (depletion mode) operation of the devices has been explained by proton transfer from the acid to the polythiophene.[36] Such acid-base reactions are well-known in polymers[37] or oligomers.[38] Their impact on the device characteristics can be understood in the following way (for the sake of simplicity assuming a negligibly small voltage drop between source and drain in the explanation): When applying no voltage between gate and source (V_{GS}), the proton transfer induces mobile (vide infra) holes in the channel in analogy to the doping of the chemically related poly(3,4-ethylenedioxythiophene) (PEDOT) by protons of the acidic poly(styrenesulfonate) (PSS).[39] The charge of these holes exactly compensates the (immobile) negative space charge layer originating from the acid residues. Applying negative V_{GS} then results in the accumulation of more holes, while a positive V_{GS} is needed to deplete the channel. One can view the situation also purely "electrostatically": If the space-charge layer due to the acid residues was not compensated by holes, it would induce opposite charges in the gate electrode. This would result in a potential drop over the dielectric in analogy to the situation in a plate capacitor putting the channel at a significantly different potential than the gate. This gives rise to carrier accumulation in the channel[25] equivalent to

what would happen, if a voltage equal to the potential drop over the gate dielectric had been applied to the gate in the absence of any space charges.

Such acidic interfacial layers hold high promise for tuning the functionality of organic electronic devices. They allow the fabrication of chemo-responsive OTFTs detecting the presence of bases like ammonia that compensate the acid doping.[36,40] They can also be used for a controlled chemical tuning of V_{th} over more than 80 V in rr-P3HT based OTFTs containing acidic SAM.[41] Beyond that, some of us have recently used photo-acid polymers as interface modification layers to control the growth of organic layers[4] and to photo chemically tune V_{th}.[11] The latter paves the way for the straightforward photolithographic production of inverters and potentially also more complex electronic circuits. Beyond that, protons at the semiconductor-dielectric interface have been found to play a decisive role for the bias-stress in OTFTs[42,43] and it has been suggested that their production upon bonding of silanes to SiO_x also impacts the device characteristics.[44]

In several of the above examples, pentacene has been used as the active material. In contrast to the situation for P3HT, where the interaction with the acid can be viewed in analogy to doping in PEDOT/PSS (vide supra), for pentacene it is much less clear, what the actual processes are that result in threshold voltage shifts due to the presence of an acid at the interface between the dielectric and the semiconductor. Clarifying that is of distinct relevance and, therefore, the topic of the present paper. In particular, we will provide evidence (i) that the main origin of the acid-induced V_{th} shift is the formation of a space-charge layer at the interface, (ii) that the V_{th} shift is the result of an acid base reaction, (iii) that the pentacene molecules are involved in that reaction, (iv) that it is the central carbon atoms of the pentacene molecules (i.e., those at the 6 and 13 positions) that are subject to protonation and (v) that the protonation results in the formation of free holes. This is achieved by combining a number of

experimental investigations on different types of OTFTs with drift-diffusion based device modelling and quantum-mechanical simulations.

2. Results and discussion

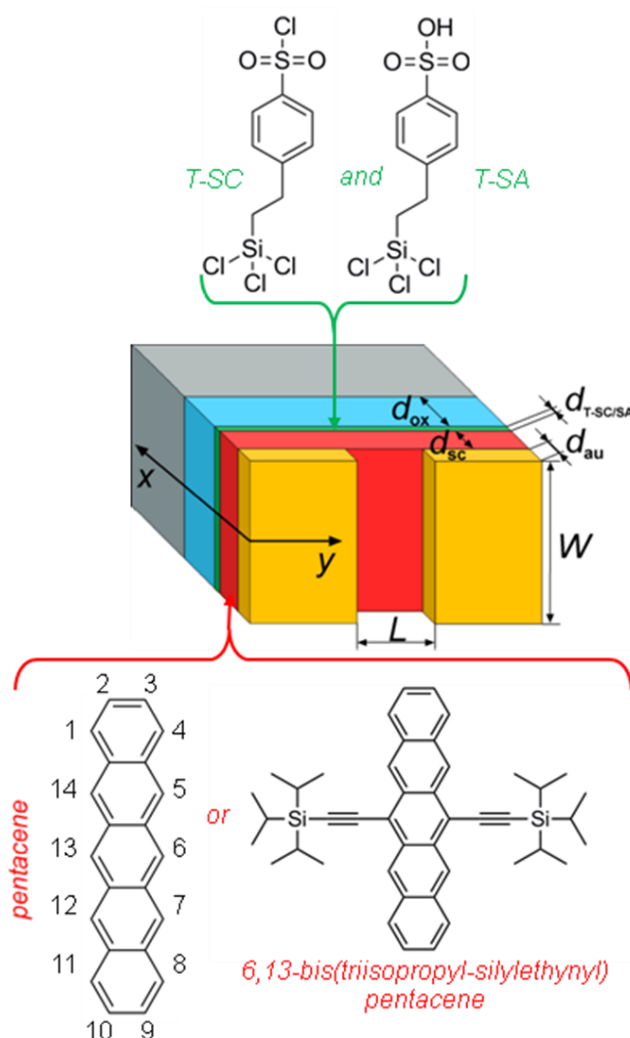

Figure 1. *Schematic structure of the investigated top-contact bottom-gate device structure, with channel lengths of L = 50 µm or L = 25 µm and a channel width of W = 7 mm. The orientation of the axes is such that a direct comparison with Fig. 5 showing the potential landscape is possible. The source and drain contacts are made of gold (Au) with a thickness of* d_{au} *= 50 nm. The active layer material is either pentacene or 6,13-bis(triisopropylsilylethynyl)pentacene (TIPS-pentacene) with a layer thickness of* d_{sc} *= 35 nm or* d_{sc} *= 56 nm, respectively. The positions at which pentacene can be protonated are*

numbered to ease discussions later in the manuscript. The semiconductor-dielectric interface layer is a blend of the two functional trichlorosilanes, T-SC and T-SA, and its thickness is in the range of 1 nm ($d_{T\text{-}SC/SA}$). Thermally grown silicon oxides with thicknesses of d_{ox} = 102.2, d_{ox} = 147.5 nm, d_{ox} = 152.0 and d_{ox} = 245.0 nm are used as the dielectric.

The schematic structure of the investigated devices is shown in Fig. 1. We used pentacene and 6,13-bis(triisopropylsilylethynyl)pentacene (TIPS-pentacene) as the active layer. The OTFTs were fabricated on doped silicon substrates with a SiO_x dielectric that has been modified using a blend of two functionalized trichlorosilanes namely 4-(2-(trichlorosilyl)ethyl)benzene-1-sulfonyl chloride (T-SC) and its sulfonic acid derivate 4-(2-(trichlorosilyl)ethyl)benzenesulfonic acid (T-SA).

2.1. Varying the thickness of the oxide layer

To separate the effects of dipole and space-charge layers, we followed a suggestion from Ref. [25], where it has been shown that, when dipolar layers are responsible for the V_{th} shift, it should be independent of the capacitance per unit area (c_{ox}) of the gate dielectric. When caused by a space charge layer, V_{th} should, however, scale linearly with the inverse of c_{ox}. This can be simply understood when viewing gate electrode, dielectric, and channel as a plate capacitor (vide supra). For a given space charge, the potential drop in that capacitor and, thus (for a given gate potential) the potential of the channel is linearly proportional to the oxide thickness, d_{ox}. Therefore, we fabricated transistors with gate oxides of varying thickness.

Exemplary transfer characteristics of (Si|SiO_x|T-SC/SA|pentacene|Au) OTFTs on oxides with nominal thicknesses $d_{ox\text{-}n}$ of 100 nm, 150 nm, and 250 nm are shown as solid squares in the three panels of Fig. 2.

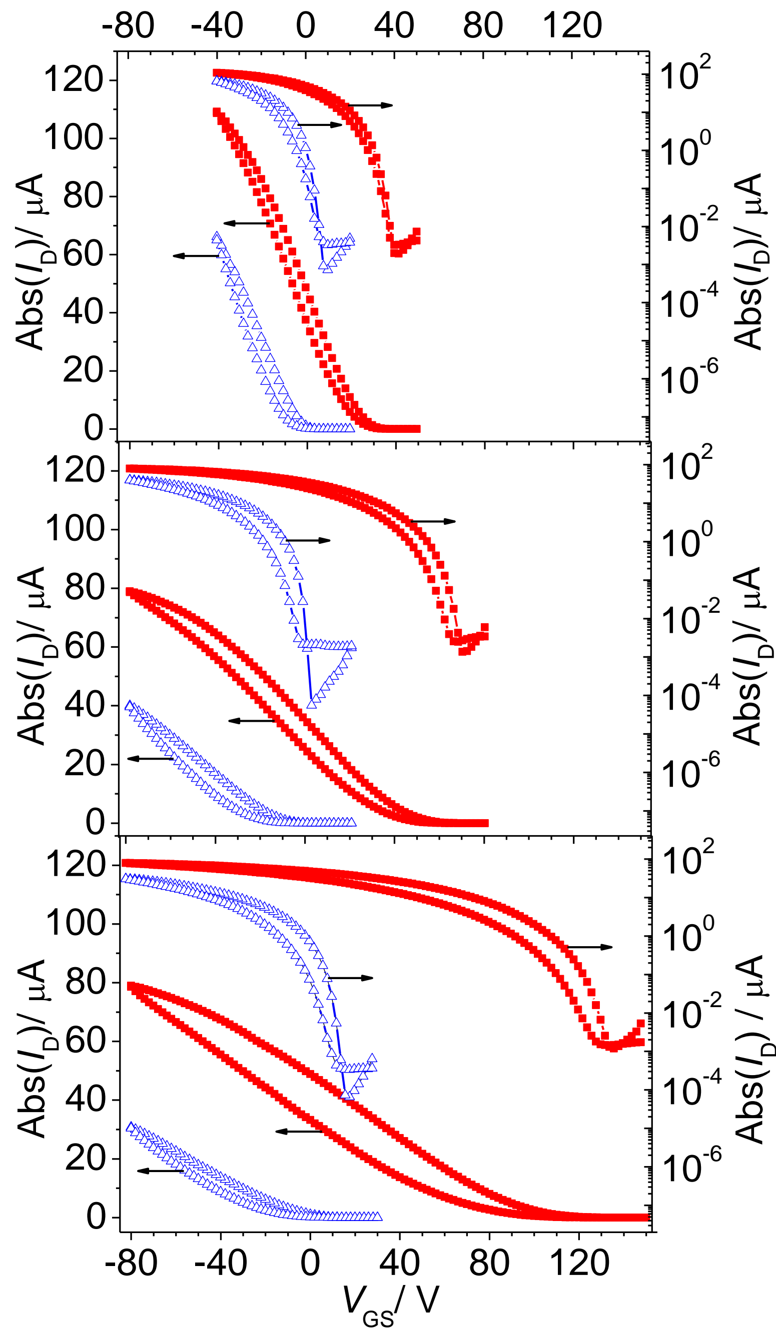

Figure 2. *Exemplary transfer characteristics of pentacene based devices including a T-SC/SA semiconductor-dielectric interface layer with nominal (actual) oxide thicknesses of* $d_{ox\text{-}n}$ *= 100 nm* (d_{ox} *= 102.2 nm),* $d_{ox\text{-}n}$ *= 150 nm (* d_{ox} *= 147.5 nm), and* $d_{ox\text{-}n}$ *= 250 nm (*d_{ox} *= 245.0 nm). Solid squares correspond to devices before and open triangles to devices after exposure to a flow of pure* NH_3 *gas. The source-drain voltage (*V_{DS}*) was set to -2 V. The increased hysteresis in the bottom plot is primarily a consequence of the extended measurement range. Further data are found in the Supporting Information.*

In all devices, high, positive V_{th} are observed, which increase with d_{ox}. Prior to further analysing these data, the layer structures of the device shall be characterized in more detail. As a first step, the relevant layer thicknesses, d_{ox} and $d_{T\text{-}SC/SA}$ are determined by x-ray reflectivity (XRR) measurements. To obtain satisfactory agreement between measurements and fits (see Supporting Information), the T-SC/SA layers had to be modelled as a double layer structure, i.e. as consisting of two layers with different electron density. The obtained layer thicknesses (d), the surface root mean square (rms) roughness values (σ), and the refractive index decrements (δ) are summarized in Tab. 1.

The measured d_{ox} values deviate only slightly from the numbers provided by the wafer suppliers (i.e. $d_{ox\text{-}n}$). The $d_{T\text{-}SC/SA}$ values on the three substrates are virtually identical and in the range of what is expected for a monolayer, whose thickness has been calculated to be 0.96 nm.[40] This is insofar important as the wafers have been obtained from two different sources. We attribute the similar SAM growth to the substrate pretreatment (cf. Experimental section) and the carefully controlled growth conditions.

Table 1. *left: Thickness (d), root mean square roughness (σ) and refractive index decrement (δ) of the fitted 3-layer structure for the three different oxide thicknesses (d_{ox}); The net-thickness of the T-SC/SA layer, $d_{T\text{-}SC/SA}$, is given by the sum of $d_{T\text{-}SC/SA\text{-}1}$ and $d_{T\text{-}SC/SA\text{-}2}$. right: average water contact angles Θ_w, diiodomethane contact angles Θ_d, and surface free energies per unit area E_s. Average values obtained for two measurement series on separately prepared layers are reported (the full data set is contained in the Supporting Information).*

d_{ox} [nm]	σ_{ox} [nm]	δ_{ox} [10^{-6}]	$d_{T\text{-}SC/SA\text{-}1}$ $d_{T\text{-}SC/SA\text{-}2}$ [nm]	$\sigma_{T\text{-}SC/SA\text{-}1}$ $\sigma_{T\text{-}SC/SA\text{-}2}$ [nm]	$\delta_{T\text{-}SC/SA\text{-}1}$ $\delta_{T\text{-}SC/SA\text{-}2}$ [10^{-6}]	$d_{T\text{-}SC/SA}$ [nm]	Θ_d [°]	Θ_w [°]	E_s [mJ*m^{-2}]
102.2	0.46	73.0	0.7 0.3	0.10 0.24	36.0 46.0	1.0	35.5	62.0	52.6
147.5	0.43	73.0	0.7 0.3	0.10 0.24	36.0 46.0	1.0	36.4	65.9	50.3
245.0	0.48	73.0	0.7 0.4	0.10 0.25	36.0 46.0	1.1	37.3	66.2	49.9

Also the contact angles of diodomethane (Θ_d) and deionized water (Θ_W) as well as the derived surface free energies per unit area (E_s) of the T-SC/SA layers are in the same range for the three samples (see Tab. 1). E_s is apparently largest for d_{ox}=102.2 nm, but the variations between the two measurement series are in the same range as the differences between the substrates.

As far as pentacene growth on the T-SC/SA layers is concerned, we find similar “over-all” morphologies on all substrates with the typical dentritic pentacene grain shape. The average grain size of the pentacene crystallites are, however, largest on the d_{ox} = 102.2 nm substrate, which has the largest E_s, as can be seen in the exemplary AFM pictures in Fig. 3. For more details see [47].

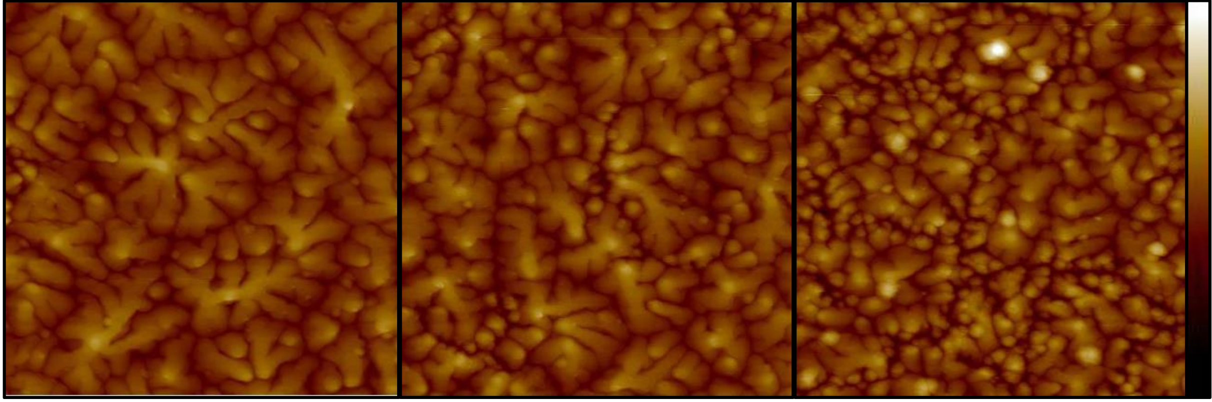

Figure 3. *AFM images showing 5 µm x 5 µm sections of 35 nm thick pentacene layers grown on T-SC/SA covered SiO_x dielectrics with d_{ox} = 102.2 nm (left), 147.5 nm (center) and 245.0 nm (right).*

Having characterized the layers, we now turn to a more detailed evaluation of the transfer characteristics shown in Fig. 2. The obtained average values for the turn-on (V_{on}) and the threshold voltages, the calculated mobilities (μ), and the on-to-off ratios (I_{on}/I_{off}) are summarized in the top part of Tab. 2. These values have been extracted from the off-to-on sweeps at a drain-source voltage (V_{DS}) of -2 V. A certain complication arises from the fact that there are a number of methods for determining V_{th} that do not necessarily yield equivalent values.[48] Therefore, we included the results obtained using the extrapolation in the linear region (ELR),[48] the second derivative method (SD),[48] and the logarithmic second derivative method (SDL).[48] The corresponding threshold voltages are denoted as V_{ELR} and V_{SD} while V_{SDL} is associated with the onset voltage, as it corresponds to the point of highest curvature in the logarithmic plots of the transfer characteristics.

Table 2. *Device parameters of (Si/SiO_x/T-SC/SA/pentacene/Au) transistors as function of different oxide thicknesses (d_{ox}) before (top part) and after NH_3 exposure (bottom part, c.f., discussion in section 2.3). Threshold/onset voltages derived with different methods, V_{ELR}, V_{SD}, and V_{SDL} (details see main text), mobilities (μ), and on to off ratios (I_{on}/I_{off}) are reported. I_{off} is*

defined as the drain current when the gate voltage equals V_{on} and I_{on} is the current for V_{GS} equaling V_{on} – 40 V. All values are average values over three different devices. A more detailed compilation of the measurement results can be found in the Supporting Information.

d_{ox} [nm]	c_{ox} [nFcm^{-2}]	V_{ELR} [V]	V_{SD} [V]	V_{SDL} [V]	μ [cm^{2}V^{-1} s^{-1}]	I_{on}/I_{off} [10^3]
102.2	34.8	20	25	38	0.24	30
147.5	23.0	39	44	65	0.12	20
245.0	14.1	90	98	136	0.13	2

d_{ox} [nm]	c_{ox} [nFcm^{-2}]	$V_{ELR-NH3}$ [V]	V_{SD-NH3} [V]	$V_{SDL-NH3}$ [V]	μ_{NH3} [cm^{2}V^{-1}s^{-1}]	$(I_{on}/I_{off})_{NH3}$ [10^3]
102.2	34.8	-5	1	8	0.22	60
147.5	23.0	-16	-9	3	0.11	90
245.0	14.1	-9	-3	20	0.12	40

In Ref. [48] the SD method, where V_{th} is associated with the maximum of the second derivative of the I_D with respect to V_G, has been suggested for extracting V_{th}. In a few of our devices, we, however, observe a relatively constant curvature of the transfer characteristics over a relatively wide voltage range in spite of the only very small applied V_{DS} of -2 V. We also often suffer from a relatively poor signal to noise ratio when calculating the numerical second derivative. In contrast, the ELR method can be readily applied and appears reasonable considering the relatively wide voltage range over which I_D depends linearly on V_{GS} (see Fig. 2). Also the reported μ values have been calculated for that region.

The devices with d_{ox} = 147.5 and d_{ox} = 245.0 nm show similar μ. The latter nearly doubles for d_{ox} = 102.2 nm consistent with the large size of the pentacene crystals (see Fig. 3).[4,46,49,50] As

shown in Fig. 4., all extracted voltages increase close to linearly with d_{ox} and thus also with $1/c_{ox}$.[51] From what has been discussed above, this indicates that the formation of a space-charge layer is the primary cause for the V_{th} shift. Interestingly, however, for all fitted lines we obtain an intercept with the V_{th}-axis at negative voltages of -32 V (ELR), -30 V (SD) and -35 V (SDL). The magnitude of this "voltage offset" is clearly larger than the estimated standard deviation for the intercept of about 5 V extracted for the three fit functions. The fit to the V_{on} (equalling V_{SDL}) is, naturally, "compromised" by the sub-threshold swing and the values of V_{ELR} and V_{SD} suffer from the ambiguity of the threshold-voltage determination. Nevertheless, this non-zero axis intercept suggests that part of the d_{ox}-dependent V_{th} shift arising from space-charge layer is, as a secondary effect, compensated by a dipole layer.

This offset is significantly larger than what one would expect from the difference in work functions of the gate electrode and the semiconductor material. A certain contribution also comes from the intrinsic molecular dipoles of the T-SC/SA molecules that have been calculated to be a few Debye resulting in potential shifts of a few volts.[36] The bond-dipole due to the binding of the silanes to the dielectric surface should additionally somewhat influence the situation. All these effects can, however, not fully explain the magnitude of the dipole-induced shift. Possible origins of the necessary "extra" dipole could be trapped protons that did not react with the pentacene (vide infra), or also trapped holes. Note that it follows from basic electrostatics that positive charges trapped above the negatively charged acid residues should not be considered as a space charge layer with a d_{ox}-dependent impact. As long as their density is smaller than that of the negatively charged acid residues they rather form a charged double layer (i.e. a dipole layer) with part of the negative charges from the acid residues. This makes their impact independent of d_{ox}.

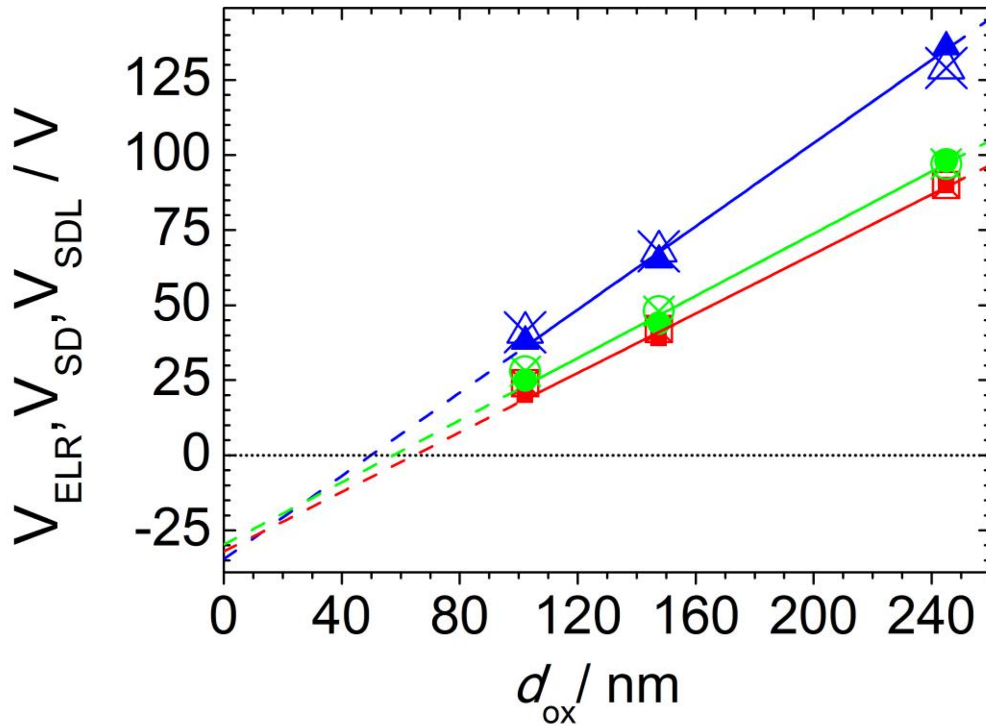

Figure 4. *Dependence of V_{ELR} (solid squares), V_{SD} (solid circles) and V_{SDL} (solid triangles) on d_{ox} for devices with three different d_{ox}. The plotted solid symbols correspond to the average experimental values, the solid lines are linear fits and the open symbols have been extracted from the results of drift-diffusion based modelling. They have been obtained by applying the same procedures used for analysing the experimental data (see main text) also to the simulated transfer characteristics.*

2.2 Results of drift-diffusion based device simulations

The above described situation is fully consistent with the results of drift-diffusion based simulations. Assuming an uncompensated negatively charged interfacial space charge layer with an areal space-charge density of -1.5 10^{17} em^{-2} and a dipole layer with a dipole density corresponding to a potential jump of -31 V, the experimental trend for V_{th} can be fully reproduced (see open symbols in Fig. 4). The above space charge density corresponds to about 12 % of the acid groups being deprotonated assuming a molecular density at the

interface of 1.3×10^{18} m^{-2} (i.e., 1/3 of the molecular packing density of the SAM obtained when assuming a 25 Å^2 footprint in this way accounting for the T-SC/T-SA ratio in the used sample)

To fully reproduce the measured transfer characteristics, a relatively complex model including different types of traps (to reproduce the sub-threshold swing and the hysteresis) as well as a mobility depending on d_{ox} to account for the different experimentally observed film morphologies needs to be employed. The results from these simulations have been used for the data in Fig. 4 and are contained in the Supporting Information. To understand the fundamental processes responsible for the V_{th} shifts, it is, however, advisable to discuss the situation within a simplified model, disregarding traps and assuming a constant mobility in all devices. The resulting potential distributions in the device at V_{DS} = -2 V for the three d_{ox} values are shown in Fig. 5 (a).

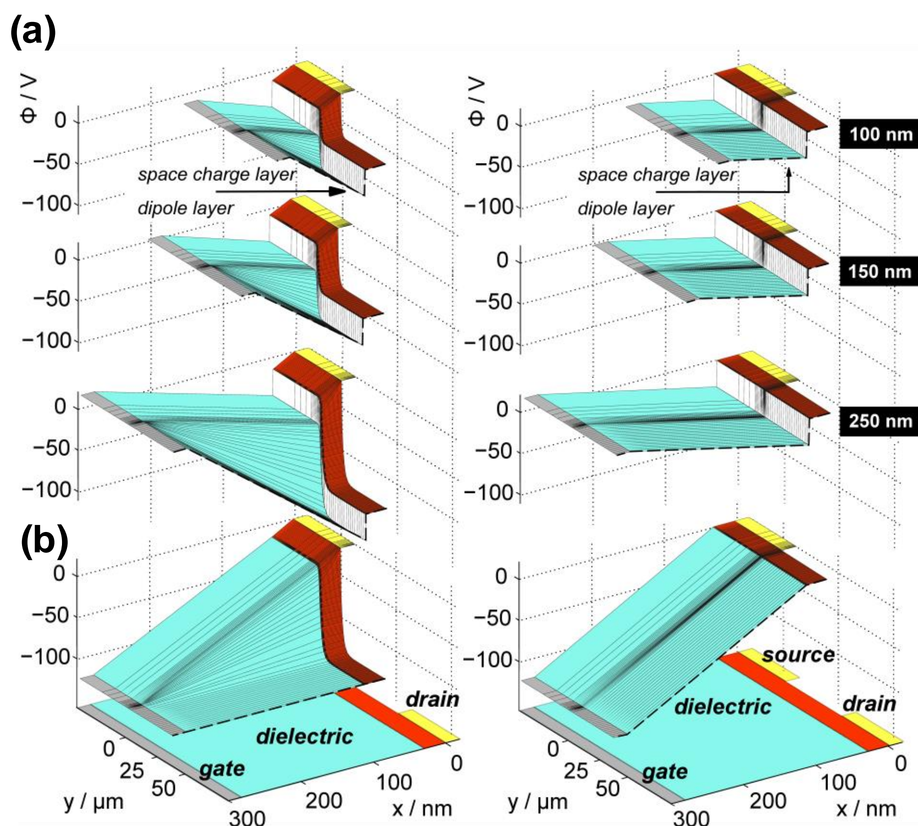

Figure 5. *(a) Simulated potential distributions for devices with a fixed negative space charge layer and a fixed dipole layer at the semiconductor-dielectric interface for oxide layer thicknesses* d_{ox} *= 100 nm, 150 nm, 250 nm. Shown is the situation in the absence of mobile charges (left column) and for the steady state (right column) in the linear regime (*V_{DS} *= -2V). The gate biases* V_{GS} *are chosen to induce the same total amount of accumulated charges in the steady state (*I_{DS} *= 81 μA) for all oxide thicknesses, (*V_{GS} *= -12.5 V, -3.3 V, and 15.3 V). To prevent obscuring important details, we omit showing the potential in the "drain-region" of the device; the position of the corresponding cut in the profiles is indicated by a broken line.*
b) Potential distribution for a device with d_{ox} *= 250 nm without an interfacial layer at the same drain current as in (a). Additionally the cross-section of the device is shown schematically. Grey areas represent the gate electrode, cyan ones the dielectric, red ones the semiconductor and yellow ones the source and drain electrodes. The position of the dipole and space-charge layers is indicated by the arrows.*

The left panels depict the situation immediately after applying the voltages, while the right panels show the steady-state situation. The gate bias V_{GS} is chosen such (i) that all devices operate in the linear regime and (ii) that the same total steady-state current (here arbitrarily set to I_{DS} = 81 μA) is achieved for all oxide thicknesses. This corresponds to V_{GS} = -12.5 V, -3.3 V, and 15.3 V, for d_{ox} = 100 nm, 150 nm, and 250 nm, respectively. Discussing a situation with I_{DS}=const represents a more general situation than merely discussing the onset regimes. The latter, however, can be easily recovered by setting I_{DS} = 0 A. Note that for $I_{DS} \neq 0$, the differences in the associated V_{GS} do not directly correspond to the offsets in V_{th}, as in the transfer characteristics also the slope of the $I_{DS}(V_{GS})$ curves is proportional to the capacitance of the dielectric (i.e., inversely proportional to d_{ox}).

To illustrate the impact of the space charge and dipole layers on the potential distribution, we first discuss the situation for the instant the external voltage is applied (i.e., before mobile charges are injected). In that case, gate, drain, and source electrodes are set to a fixed potential and no mobile charges are in the device. Without space charges or dipoles at the interface (see Fig. 5 (b)), the potential in the pentacene volume that is not covered by source or drain electrodes ($0 < y < 50$ μm) assumes the value of the gate potential. This is a consequence of the huge aspect ratio of the considered transistors (channel length of 50 μm vs. an overall thickness of the active region and dielectric between 135 nm and 285 nm).[25] Further, the potential drops linearly from the source/drain electrodes to the gate electrode ($y \leq 0$, 50μm $\leq y$) with different slopes in the semiconductor and the dielectric as dictated by their dielectric constants.

The situation in the channel region not covered by the source- and drain electrodes is significantly modified in the presence of the interfacial space charges and dipole layers. Due to the space charge layer, there is an additional voltage drop across the dielectric layer (Fig. 5 (a), left panels). The corresponding electric field in the oxide layer is the same for all oxide thicknesses as a consequence of comparing situations with equivalent drain currents in the steady-state (vide supra). The extent of the potential drop increases linearly with d_{ox}, reminiscent of the situation in a plate capacitor. The potential step at the interface due to presence of the dipole layer partly counteracts the potential drop over the oxide. Since the height of this step is, however, solely determined by the dipole density, it is independent of d_{ox}.

Underneath the source and drain electrodes, a different situation is encountered: Here, the total potential difference is given by V_{GS} and V_{GD}, respectively. As a consequence, there is a

potential drop over the pentacene layer (unlike in the channel region far from source and drain described in the previous paragraph). For the three situations depicted in Fig. 5 (a), this potential drop is independent of d_{ox}. This follows from the requirement that for the steady state all drain currents are identical. The same requirement explains why also the field in the oxide does not depend on d_{ox}. This then results in the observed d_{ox} dependent potential drop over the oxide that is offset by the potential discontinuity due to the dipole layer.

For reaching the steady state (Fig. 5 (a), right panels), charges are injected from the source electrode and accumulate in the channel region. As a consequence, in the regions underneath the contacts the potential in the pentacene layer is fixed to the source and drain potentials. I.e., there is neither a field in the x- nor in the y-directions. Also in the part of the device not covered by the electrodes, the field in the x-direction vanishes, but there is a steady potential drop in the y-direction as a consequence of the applied V_{DS} (as the latter is chosen to be only -2 V here, this potential drop is, however, not well resolved in Fig. 5). Because we compare the situation of identical I_{DS}, the accumulated hole density at the semiconductor/dielectric interface is the same for all d_{ox}, which also renders the field in the oxide identical.

2.3 Dedoping by ammonia and bulk doping using hydrochloric acid

To determine, whether the V_{th} shift is a consequence of an acid-base reaction, we performed two test experiments: First, we exposed the devices containing the T-SC/SA layers to a base as the latter should neutralize the acid; for that purpose we chose NH_3 gas and exposed the devices for 30 min to ensure that an equilibrium situation is established (details see Experimental section and Supporting Information). This exposure results in a substantial shift of V_{th} to less positive values with the total shift being essentially proportional to d_{ox} (see Fig. 2). As a result, the V_{th} values of all devices after NH_3 exposure become similar. In analogy to

what has been described in[36,40] for P3HT based devices, this shift can be explained by a neutralization of the acidic groups of the T-SA molecules by NH_3 resulting in the formation of the electronically inactive ammonium 4-(2-(trichlorosilyl)ethyl)benzenesulfonate as shown for pristine T-SC/SA layers by various spectroscopic techniques.[40] Interestingly, the I_{off} are in the same range before and after NH_3 exposure. For more details see Ref. [52].

In a second test experiment, we exposed (Si|SiO$_x$|pentacene|Au) devices, i.e., devices not containing a T-SC/SA interfacial layer, to HCl gas. The resulting device characteristics are shown in Fig. 6.

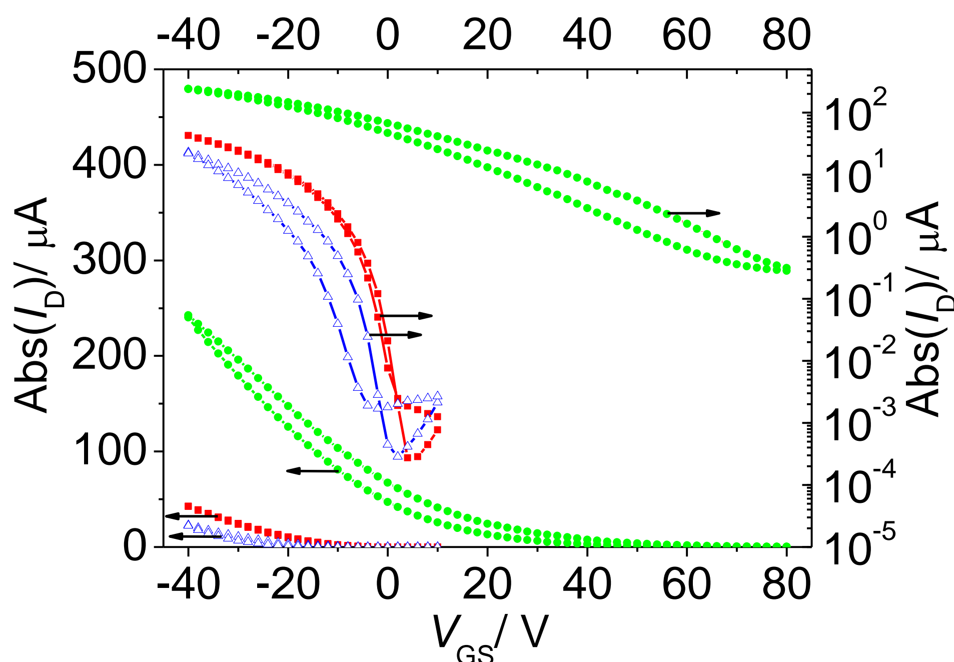

Figure 6. *Transfer characteristics of an exemplary (Si/SiO$_x$/pentacene/Au) device with d_{ox} = 152.0 nm (solid squares), after exposure to HCl vapour (solid circles) and after subsequent exposure to NH_3 (open triangles). V_{DS} is set to -2 V.*

Very much like in the devices containing an acidic interfacial layer, exposure to HCl vapor results in highly positive V_{th} and V_{on}. This shift to positive V_{th} is stable over days when keeping the devices in an Ar-glove box, which indicates a strong chemical interaction

between pentacene and the HCl molecules, because otherwise HCl would gradually diffuse out of the device. The fact that again V_{on} can be shifted back to around zero upon exposure of the device to NH_3 gas (see open triangles in Fig. 6) shows that also here we are dealing with acid-base reactions. This is consistent with the notion that bulk doping of the active layer material shifts V_{th} as derived on the basis of analytic equations[31-33] and by drift-diffusion based simulations.[25,34,35]

Thus, we propose a protonation of some of the pentacene molecules in the active layer upon interaction with a strong enough acid (HCl vapour or the T-SC/SA interface layer). Protonation of pentacene molecules in the gas phase has, indeed, been suggested by quantum chemical simulations[53,54] and by several different experimentally measurements, namely by Fourier transform ion cyclotron resonance mass spectrometry,[53] IR and IR multiple-photon dissociation spectroscopy.[55] The experiments presented above are a strong indication that analogous reactions occur also in the solid state.

Interestingly, the exposure to HCl vapour in several of the investigated devices resulted in a deterioration of the I_{on}/I_{off} ratio as a consequence of a significant increase of I_{off}. This is in clear contrast to the insertion of the T-SC/SA layer as shown in Fig. 2. It should, however, be mentioned that the measured values of I_{off} upon exposure to HCl display a significant device-to-device variation as shown in the Supporting Information.

A possible explanation for the increased I_{off} in Fig. 6 is that exposure to HCl vapor induces proton-transfer doping throughout the whole film, while it is reasonable to assume that the use of an interfacial layer (like T-SC/SA) primarily affects the region close to the semiconductor-dielectric interface. In literature[56] it has indeed been suggested that bulk doping results in an increased off current. This, is, however, cast into doubt by Refs. [34,35], where it is argued

that such an increase of the I_{off} is a consequence of traps, while bulk doping without trap creation (albeit at a much lower concentration than in [50]) only results in a shift of V_{th}.

2.4 Acid-base reactions in TIPS-pentacene based devices

To clarify, which part of the pentacene molecule is actually affected by the protons of the acid, it is useful to consider the proton affinity (PA) of the various carbon positions. Calculations in Ref. [53,54] indicate that the two carbon atoms of the central ring in pentacene have the highest PA. Our quantum-chemical simulations at the B3LYP/6-31G(d,p) level indeed confirm that the protonation of pentacene at the central 6 position is energetically favoured by 0.87 eV (resp. 0.74 eV and 0.15 eV) over a protonation at the 3 (resp. 4 and 5) positions (the numbering of the carbon atoms in the pentacene backbone is included in Fig. 1).

To test experimentally, whether this is the case in the solid state, we performed comparative studies using a suitably modified pentacene derivative as the active semiconductor material: In TIPS-pentacene (chemical structure see Fig. 1), the central two carbon atoms of pentacene are substituted by triisopropyl(prop-1-yn-1-yl)silane, which can be expected to very significantly modify their proton affinity. Indeed, already when fully optimizing the structure of a protonated TIPS-pentacene molecule (corresponding to the gas phase), the energetic "advantage" of the 6 over the 3 position is reduced to 0.48 eV (0.37 eV for the 4 position; protonation at the 5 position is, in fact, energetically favoured here by 0.25 eV). Moreover, primarily due to a change in hybridisation of the protonated carbon atom, the structure of the molecule is heavily distorted as shown in the Supporting Information. Such a distortion will not happen in the solid state, especially in a highly crystalline,[57] densely packed layer. Thus,

we also calculated the total energy of a protonated TIPS-pentacene molecule, in which the central part of the backbone was forced to remain planar. In this case, protonation at the central carbon atom becomes energetically more *costly* by 0.37 eV (resp., 0.48 eV and 1.10 eV) than protonation at the 3 (resp. 4 and 5) positions. These data shows that due to the substitution protonation at the central carbon atoms can be excluded in a TIPS-pentacene film.

Thus, if the above described high positive V_{th} upon insertion of a T-SC/SA layer or exposure to HCl vapor were, indeed, the consequence of a protonation of the central pentacene carbon atoms, they should not occur when using TIPS-pentacene as the active material. This is exactly what we observe in the corresponding test experiments, where *neither the inclusion of a T-SC/SA layer nor the exposure to HCl vapor gives rise to any shift in* V_{th} (for transfer characteristics see the Supporting Information). This can be considered as convincing evidence that (i) the acid-induced V_{th} shifts in pentacene-based devices are a consequence of a chemical reaction between the acid and the active material and not, e.g., due to an interaction with silanole surface groups or related species; and that (ii) the position of protonation in pentacene is at the central carbon atom.

2.5 The suggested mechanism for surface proton transfer doping in pentacene based OTFTs

The above results lead us to suggest the mechanism depicted in Fig. 7 for surface proton transfer doping in pentacene based OTFTs: A fraction of the pentacene molecules close to the interface with the T-SC/SA layer are protonated. This fraction remains relatively small, as can be inferred from the drift-diffusion based modelling (vide supra). Such a situation is consistent with the protonation being an endothermal process rendering the reaction entropy-driven. The positive charge on the pentacene molecule originating from the proton transfer is

then transferred to a neighbouring molecule. This is necessary to explain the experiments, as otherwise one would be dealing with trapped rather than mobile holes as a result of the proton-transfer doping process.

It is also consistent with our quantum-chemical simulations, as the charge transfer to a non-protonated pentacene results in an energy gain of ~0.60 eV. This value is obtained from the comparison of the B3LYP/6-31G(d,p) calculated ionization potentials of pentacene and the pentacene-6-ylium (for chemically structure see Fig. 7) with an additional proton at the central position and assumes equivalent screening in both. The reason for the increased ionization potential of the molecule bearing the extra proton is the disrupted conjugation by the central sp^3 hybridized carbon atom. As a consequence, pentacene-6-ylium molecules will no longer participate in the hole transport at the interface, but they will also not act as traps. Thus, the carrier mobility should not be reduced by the protonation of a small fraction of the pentacene molecules, which is again consistent with the experiments. Considering the increased reactivity of pentacene-6-ylium molecules in situation (c) of Fig. 7 due to their radical character, it cannot be excluded that these molecules are actually subject to a second protonation process, but we have no clear evidence for it to actually happen.

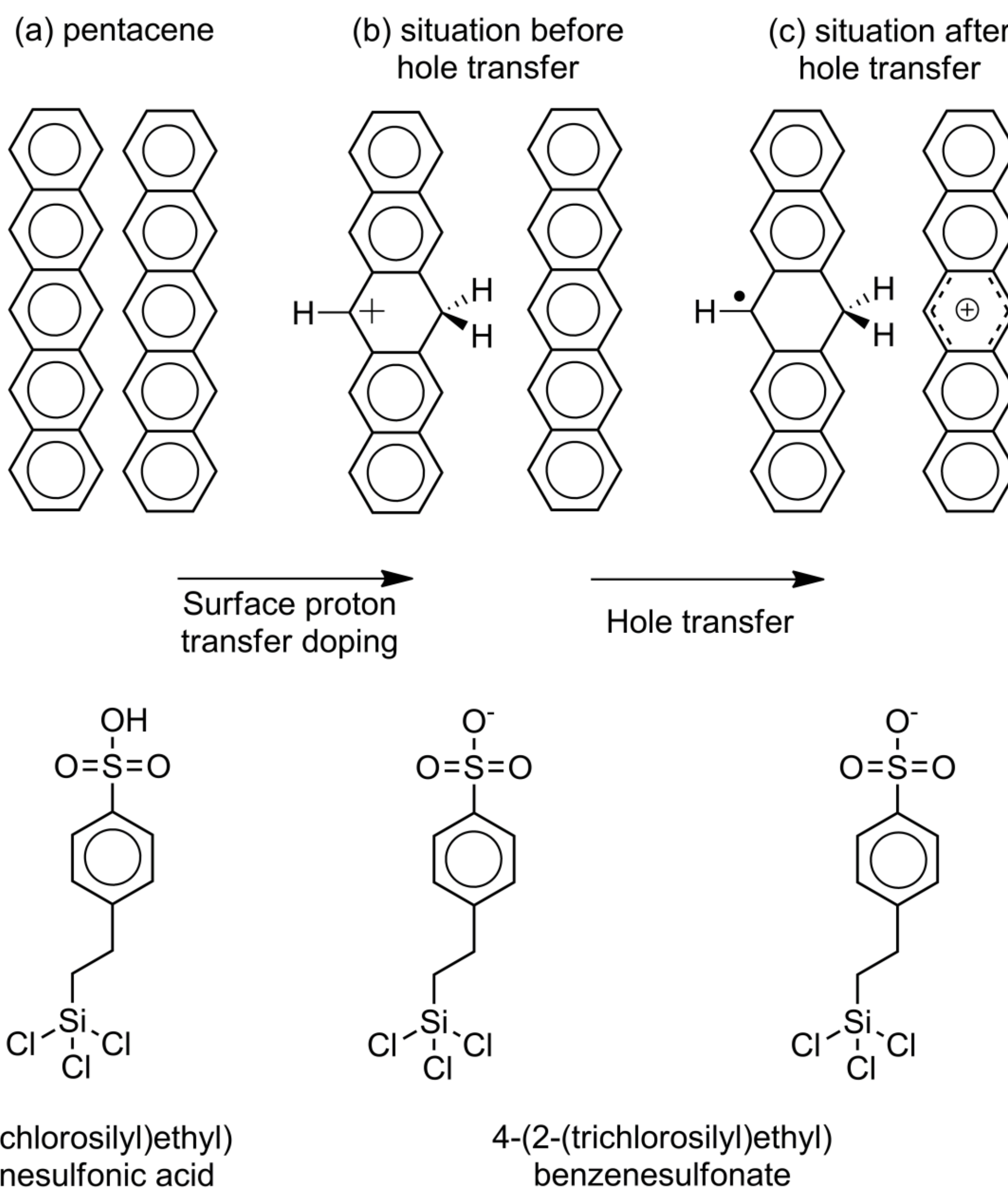

Figure 7. *Suggested mechanism for surface proton transfer doping of pentacene by the protons of the sulfonic acid functionalities of the T-SA molecules. (a) shows the situation before doping. (b) shows a protonated pentacene molecule (pentacene-6-ylium); the resulted disruption of the conjugation results in the positive charge being transferred to a neighbouring molecule, forming a free hole (c).*

2.6 Establishing equilibrium and the role of ambient light

Finally, it should be noted that the high positive V_{th} values induced by a T-SC/SA layer and depicted in Fig. 2 develop only gradually. I.e., for devices stored in the glove-box in light (i.e., without any intentional darkening), it takes several days until a stable situation is reached that also does not change under the measurement conditions described below. In contrast, the equilibrium is established instantaneously, when performing the doping experiments using HCl vapour. This can be attributed to the abundance of HCl molecules when exposing the devices to HCl vapour. Interestingly, we saw immediate doping also when using two types of polymeric interfacial layers that consist of photo acids.[11] We attribute this to the fact that in these experiments, to form the acids, we illuminate the samples by UV-light and it is known for several organic systems that their acidity is much higher, when the molecules are in the excited state.[58-61]

In fact, also for doping with a T-SC/SA interfacial layer, the exposure to light impacts the steady-state situation. When storing a device in darkness for a month right after fabrication, the achieved positive V_{th} were clearly smaller than in a control device stored under ambient light. When the latter device is then kept in darkness for several days, its V_{th} shifts back to the value measured for the device never exposed to ambient light. This could be a consequence of a shift in the chemical equilibrium of the reactions depicted in Fig. 7 upon illumination.

On the other hand, a “darkness-induced” shift of V_{th} to more negative values is reminiscent of the experiments by Jing et al., who observed (albeit for P3HT based devices on bare SiO_x, i.e., without any interface modifications) threshold voltages as low as -60 V when storing their devices in the dark,[62] which can be attributed to charge-carrier trapping. In that spirit, it cannot be excluded that the less positive values of V_{th} for T-SC/SA containing pentacene devices stored in the dark are due to a partial cancellation of the doping effect by charge

carrier trapping rather than a result of a shifted chemical equilibrium. To definitely answer such questions, extensive tests of the impact of light (of different wavelength) on various types of transistors containing different interface modifications and active layer materials will be necessary. This goes clearly beyond the scope of the present paper.

3. Conclusions

Combining a number of experiments with drift-diffusion based device modelling and quantum-chemical calculations, we study the mechanism responsible for the high positive threshold voltages observed in pentacene based OTFTs, where the active layer is in contact with an acid. This is of relevance as, for example, devices containing acidic layers have a high potential for realizing chemically responsive devices[63] and allow for an efficient photochemical production of depletion-load inverters.[11] The focus of the present study lies on pentacene transistors containing acidic monolayers covalently bonded to the gate dielectric. The theoretical and experimental investigation of the dependence of the monolayer-induced threshold voltage, V_{th}, shift on the thickness of the gate dielectric reveals that it is due to the formation of an interfacial space-charge layer partially compensated by the formation of a dipole layer. The fact that a similar effect can be realized by HCl exposure of devices not containing an acidic layer and the finding that the V_{th} shift can be eliminated by exposing the devices to a base (in our case NH_3) show that the observed doping is the consequence of an acid/base reaction. Interestingly, none of the above effects is observed when replacing pentacene by TIPS-pentacene. This, on the one hand, proves that it is the interaction between the acid and the active material that is responsible for the V_{th} shift and, on the other hand, points to the central two carbon atoms of pentacene being subject to the electrophilic attack by the protons. It also implies that whether or not a certain semiconductor is prone to protonation (and, thus, useful for the above mentioned applications), subtly depends on the proton affinity

of the available docking sites. These data together with results of quantum-chemical simulations finally allow suggesting the chemical and electronic mechanism sketched in Fig. 7 for surface proton transfer doping in pentacene based OTFTs.

4. Experimental

As especially the growth of the T-SC/SA layers is impacted severely by the very details of the fabrication process (especially by minute changes of the water concentration during film growth), we considered it appropriate to provide a very detailed description of the applied methodologies. Due to space limitations, they are, however, largely contained in the Supporting Information.

Device fabrication: As substrates (serving also as gate electrodes), we used doped silicon wafers with thermally grown oxides with thicknesses d_{ox} = 102.2 nm, d_{ox} = 147.5 nm, d_{ox} = 152.0 nm, and d_{ox} = 245.0 nm pre-cut into 2 cm x 2 cm pieces supplied by Siegert Consulting and Silchem. The oxide surfaces of the substrates were cleaned and activated by an oxygen plasma etching process and subsequently sonicated for 2 min in deionized water. This rendered the oxide surfaces of all samples highly hydrophilic lowering the contact angle of H_2O to below 10°, the limit of our contact-angle measurement set-up. This is important as the resulting high concentration of –OH groups on the waver surface is beneficial for the docking of silanes.[64] As a next step, T-SC/SA layers were grown on the majority of the wafers as described below. The active layer material pentacene was deposited under high-vacuum conditions typically some days after growing the T-SC/SA layer. The first 5 nm were deposited at a rate of 0.02 Å/s and the following 30 nm at a rate of 0.1 Å /s, as measured with a quartz microbalance. During pentacene-growth, the substrates were held at a temperature of

65 ° C. Alternatively, TIPS-pentacene films were deposited from a 1 wt % solution in toluene by spin coating in air with the substrate heated to 60°C using an IR lamp (spin parameters set to: 2000 rpm for 18s and 4000 rpm for 20s). The ca. 50 nm thick gold source and drain electrodes were produced at a pressure in the range of 10^{-6} mbar in a home-built evaporation set-up operated inside an Ar glove-box. Four transistors were fabricated on each substrate.

Growth of the T-SC/SA layer: After the plasma etching process and the water sonication, the substrates were further cleaned in several steps (cf. Supporting Information) and put into 10 ml highly dry toluene (water content of about 7 ppm measured with Karl Fischer Titration) inside an Ar glove-box. To that we added 10 μl of the commercial T-SC/SA solution from ABCR, which is a 50 vol % mixture of T-SC/SA molecules and toluene and let the layer grow for 16 h. After this time, the substrates were sonicated and rinsed in fresh toluene. Finally, they were annealed for 30 min at about 100 °C at a pressure of about 0.6 mbar.

The *XRR data* were recorded on a Bruker D8 Discover diffractometer using CuK_{α}-radiation and analyzed using WinGixa,[65] which is an implementation of Parratt' s recursive algorithm.[66] It includes interface, σ_{ox}, and surface roughness, $\sigma_{T\text{-}SC/SA}$, according to the approach of Nevot and Croce.[67] *Contact angles* were measured with a Kruess DSA 100 drop shape analysis system using deionized water and diiodomethane as test liquids. Based on the method by Owens Wendt,[68] the surface free energy per unit area E_s of the T-SC/SA layers were calculated automatically. AFM pictures were measured with a Veeco Dimension DI3000 in tapping mode with standard silicon tips.

To *expose the devices to NH_3 gas*, we put our devices in a homemade measurement cell and flooded the cell with NH_3 gas for either 30 min (data in Fig. 2) or 1 min (data in Fig. 6). After the NH_3 exposure, we flooded the cell with argon gas until we could not detect ammonia at

the gas outlet of the measurement cell. For *HCl*-vapor exposure, we put the ready-made devices over a beaker filled with fuming hydrochloric acid for 1 min. *Hazard warning! NH_3 is highly toxic and HCl vapor is very acidic; thus, experiments should always be performed in a fume hood using appropriate gloves and protective glasses!*

Source meter measurements: To measure the electronic characteristics of the transistors, we used a Keithley 2636A dual source-meter controlled with a home-made software. We started the transfer sweeps at positive gate bias, reduced V_{GS} in steps of -2 V (setting the delay time to 0.1 s). The reported device parameters were always determined for the sweep from positive to negative V_{GS}. All measurements were performed under ambient light inside a glove box.

Drift-diffusion based modeling:

The numerical model to describe device characteristics is a two-dimensional drift-diffusion approach as described in Ref. [25] with special boundary conditions at the source and drain electrodes. Charge carrier injection occurs via thermionic emission and tunnelling through a potential barrier (given by the image charge model) in Wenzel-Kramers-Brillouin approximation and is corrected by an interface recombination current.[69] The corresponding system of equations with appropriate boundary conditions is solved self-consistently on a non-regular two-dimensional grid[25] using an implicit time integration. A hole injection barrier of 0.47eV,[70] and dielectric constants of $\varepsilon = 3.4$ (pentacene) and $\varepsilon = 3.9$ (SiO_x) are assumed. To model interfacial charge and dipole layers areal charge distributions with fixed densities were used. To further account for the shapes of the I-V curves obtained in the experiments also two types of traps are need to be considered: (i) The occurrence of a hysteresis is simulated by including bulk traps, whose occupation is determined self-consistently for each time step. (ii) To account for the shape of the transfer-characteristics in the sub-threshold region, additional interface traps with significantly shorter time constants

are incorporated. Considerably more details on these simulations are contained in the Supporting Information.

Quantum-mechanical modelling:

The quantum-mechanical calculations were performed using Gaussian03[71] applying the B3LYP[72] hybrid functional and a 6-31G(d,p) basis set. Total energies were extracted from the last step in the geometry optimizations. Note that we encountered serious convergence problems, when optimizing the geometry of planarized TIPS-pentacene protonated at one of the central C-atoms. The way we circumvented these problems is described in the Supporting Information.

Acknowledgements

We thank A. Fian for growing the pentacene films of the transistors exposed to HCl vapor, H. Brandner for reproducing the findings of Ref. [62], Roland Resel for XRR support, and Christian Slugovc as well as Thomas Grießer for stimulating discussions. Financial support by the Austrian Science Fund (FWF): P 19959-N20 and by the Austrian Nanoinitiative (FFG and bmvit) through the NILsimtos project as part of the NILaustria cluster are acknowledged. Supporting Information is available online from Wiley InterScience or from the author.

Received: ((will be filled in by the editorial staff))

Revised: ((will be filled in by the editorial staff))

Published online: ((will be filled in by the editorial staff))

[1] X. Sun, C. Di, Y. Liu, *JOURNAL OF MATERIALS CHEMISTRY* **2010**, *20*, 2599-2611.
[2] S. A. DiBenedetto, A. Facchetti, M. A. Ratner, T. J. Marks, *Advanced Materials* **2009**, *21*, 1407-1433.
[3] L.-L. Chua, J. Zaumseil, J.-F. Chang, E. C.-W. Ou, P. K.-H. Ho, H. Sirringhaus, R. H. Friend, *Nature* **2005**, *434*, 194-199.
[4] M. Marchl, A. W. Golubkov, M. Edler, T. Griesser, P. Pacher, A. Haase, B. Stadlober, M. R. Belegratis, G. Trimmel, E. Zojer, *Appl. Phys. Lett.* **2010**, *96*, 213303.
[5] J. Koo, S. Kim, J. Lee, C. Ku, S. Lim, T. Zyung, *Synthetic Metals* **2006**, *156*, 99-103.
[6] C.-L. Fan, Y.-Z. Lin, C.-H. Huang, *Semicond. Sci. Technol.* **2011**, *26*, 045006.
[7] Y. Jang, J. H. Cho, D. H. Kim, Y. D. Park, M. Hwang, K. Cho, *Appl. Phys. Lett.* **2007**, *90*, 132104.
[8] M. Halik, H. Klauk, U. Zschieschang, G. Schmid, C. Dehm, M. Schutz, S. Maisch, F. Effenberger, M. Brunnbauer, F. Stellacci, *Nature* **2004**, *431*, 963-966.
[9] H. Ma, O. Acton, G. Ting, J. W. Ka, H.-L. Yip, N. Tucker, R. Schofield, A. K.-Y. Jen, *Appl. Phys. Lett.* **2008**, *92*, 113303.
[10] J.-M. Choi, J. H. Kim, S. Im, *Appl. Phys. Lett.* **2007**, *91*, 083504.
[11] M. Marchl, M. Edler, A. Haase, A. Fian, G. Trimmel, T. Griesser, B. Stadlober, E. Zojer, *Adv. Mater.* **2010**, *22*, 5361-5365.
[12] A. Wang, I. Kymissis, V. Bulović, A. I. Akinwande, *Appl. Phys. Lett.* **2006**, *89*, 112109.
[13] A. Wang, I. Kymissis, V. Bulovic, A. I. Akinwande, in *Electron Devices Meeting, 2004. IEDM Technical Digest. IEEE International*, **2004**, S. 381-384.
[14] H. Kawaguchi, M. Taniguchi, T. Kawai, *Appl. Phys. Lett.* **2009**, *94*, 093305.
[15] H. Sakai, Y. Takahashi, H. Murata, *Appl. Phys. Lett.* **2007**, *91*, 113502.
[16] H. E. Katz, X. M. Hong, A. Dodabalapur, R. Sarpeshkar, *J. Appl. Phys.* **2002**, *91*, 1572.
[17] H. Sakai, K. Konno, H. Murata, *Appl. Phys. Lett.* **2009**, *94*, 073304.
[18] Y. Guo, Y. Liu, C.-an Di, G. Yu, W. Wu, S. Ye, Y. Wang, X. Xu, Y. Sun, *Appl. Phys. Lett.* **2007**, *91*, 263502.
[19] S. Kobayashi, T. Nishikawa, T. Takenobu, S. Mori, T. Shimoda, T. Mitani, H. Shimotani, N. Yoshimoto, S. Ogawa, Y. Iwasa, *Nat Mater* **2004**, *3*, 317-322.
[20] K. P. Pernstich, S. Haas, D. Oberhoff, C. Goldmann, D. J. Gundlach, B. Batlogg, A. N. Rashid, G. Schitter, *J. Appl. Phys.* **2004**, *96*, 6431.
[21] K. P. Pernstich, C. Goldmann, C. Krellner, D. Oberhoff, D. J. Gundlach, B. Batlogg, *Synthetic Metals* **2004**, *146*, 325-328.
[22] *The Influence of Trap States on Charge Transport in Organic Transistors*, Eth, Zürich, **2007**.
[23] C. Huang, H. E. Katz, J. E. West, *Langmuir* **2007**, *23*, 13223-13231.
[24] M. Mottaghi, G. Horowitz, *Organic Electronics* **2006**, *7*, 528-536.
[25] S. K. Possanner, K. Zojer, P. Pacher, E. Zojer, F. Schürrer, *Adv. Funct. Mater.* **2009**, *19*, 958-967.
[26] W. Chen, D. Qi, X. Gao, A. T. S. Wee, *Progress in Surface Science* **September**, *84*, 279-321.
[27] W. Chen, X. Y. Gao, D. C. Qi, S. Chen, Z. K. Chen, A. T. S. Wee, *Adv. Funct. Mater.* **2007**, *17*, 1339-1344.
[28] J. Ristein, *Science* **2006**, *313*, 1057 -1058.
[29] P. Strobel, M. Riedel, J. Ristein, L. Ley, *Nature* **2004**, *430*, 439-441.
[30] H. Liu, Y. Liu, D. Zhu, *J. Mater. Chem.* **2011**, *21*, 3335.
[31] G. Horowitz, R. Hajlaoui, H. Bouchriha, R. Bourguiga, M. Hajlaoui, *Adv. Mater.* **1998**, *10*, 923-927.

[32] R. Tecklenburg, G. Paasch, S. Scheinert, *Adv. Mater. Opt. Electron.* **1998**, *8*, 285-294.
[33] S. Scheinert, G. Paasch, *phys. stat. sol. (a)* **2004**, *201*, 1263-1301.
[34] S. Scheinert, G. Paasch, M. Schrödner, H.-K. Roth, S. Sensfuß, T. Doll, *J. Appl. Phys.* **2002**, *92*, 330.
[35] S. Scheinert, G. Paasch, T. Doll, *Synthetic Metals* **2003**, *139*, 233-237.
[36] P. Pacher, A. Lex, V. Proschek, H. Etschmaier, E. Tchernychova, M. Sezen, U. Scherf, W. Grogger, G. Trimmel, C. Slugovc, E. Zojer, *Adv. Mater.* **2008**, *20*, 3143-3148.
[37] B. J. Polk, K. Potje-Kamloth, M. Josowicz, J. Janata, *The Journal of Physical Chemistry B* **2002**, *106*, 11457-11462.
[38] C. W. Spangler, L. Picchiotti, P. Bryson, K. O. Havelka, L. R. Dalton, *J. Chem. Soc., Chem. Commun.* **1992**, 145.
[39] In aqueous dispersion (PEDOT:PSS) it is a commercial product of H. C. Starck GmbH, Germany, http://www.hcstarck.de.
[40] P. Pacher, A. Lex, V. Proschek, O. Werzer, P. Frank, S. Temmel, W. Kern, R. Resel, A. Winkler, C. Slugovc, R. Schennach, G. Trimmel, E. Zojer, *The Journal of Physical Chemistry C* **2007**, *111*, 12407-12413.
[41] H. Etschmaier, P. Pacher, A. Lex, G. Trimmel, C. Slugovc, E. Zojer, *Appl. Phys. A* **2008**, *95*, 43-48.
[42] A. Sharma, S. G. J. Mathijssen, M. Kemerink, D. M. de Leeuw, P. A. Bobbert, *Appl. Phys. Lett.* **2009**, *95*, 253305.
[43] A. Sharma, S. G. J. Mathijssen, E. C. P. Smits, M. Kemerink, D. M. de Leeuw, P. A. Bobbert, *Phys. Rev. B* **2010**, *82*, 075322.
[44] D. Boudinet, M. Benwadih, S. Altazin, J.-M. Verilhac, E. De Vito, C. Serbutoviez, G. Horowitz, A. Facchetti, *Journal of the American Chemical Society* **2011**, *133*, 9968-9971.
[45] S. Y. Yang, K. Shin, C. E. Park, *Advanced Functional Materials* **2005**, *15*, 1806-1814.
[46] W.-Y. Chou, C.-W. Kuo, H.-L. Cheng, Y.-R. Chen, F.-C. Tang, F.-Y. Yang, D.-Y. Shu, C.-C. Liao, *Appl. Phys. Lett.* **2006**, *89*, 112126.
[47] In Ref. [4] the largest grain sizes have been observed for the smallest E_s, resulting in the highest μ. But in Ref. [45] they observe a correlation between high E_s and large crystals, but low μ and in Ref. [46] high E_s correlated with small grain size and results in low μ. This indicates that the correlation between grain size, E_s and μ is still unclear.
[48] D. Boudinet, G. Le Blevennec, C. Serbutoviez, J.-M. Verilhac, H. Yan, G. Horowitz, *J. Appl. Phys.* **2009**, *105*, 084510.
[49] A. Di Carlo, F. Piacenza, A. Bolognesi, B. Stadlober, H. Maresch, *Appl. Phys. Lett.* **2005**, *86*, 263501.
[50] R. Matsubara, N. Ohashi, M. Sakai, K. Kudo, M. Nakamura, *Appl. Phys. Lett.* **2008**, *92*, 242108.
[51] In this context it needs to be mentioned that c_{ox} is not exactly inversely proportional to d_{ox} as the SAM represents an additional capacitance in series. Considering, however, that $d_{T-SC/SA}$ amounts to less than 1% of the overall thickness of all dielectrics and that its dielectric constant is roughly one third of that of SiO_x its influence can be safely neglected.
[52] The relatively high I_{off} values in our experiments are a consequence of the used 2 cm x 2 cm substrates holding several devices with a common gate structure.
[53] R. Notario, J.-L. M. Abboud, *The Journal of Physical Chemistry A* **1998**, *102*, 5290-5297.
[54] A. Knežević, Z. B. Maksić, *New J. Chem.* **2006**, *30*, 215.
[55] H. Knorke, J. Langer, J. Oomens, O. Dopfer, *ApJ* **2009**, *706*, L66-L70.
[56] A. R. Brown, C. P. Jarrett, D. M. de Leeuw, M. Matters, *Synthetic Metals* **1997**, *88*, 37-55.
[57] J. E. Anthony, J. Gierschner, C. A. Landis, S. R. Parkin, J. B. Sherman, R. C. Bakus II, *Chem. Commun.* **2007**, 4746.

[58] L. M. Tolbert, K. M. Solntsev, *Acc. Chem. Res* **2002**, *35*, 19-27.
[59] N. Agmon, *The Journal of Physical Chemistry A* **2005**, *109*, 13-35.
[60] L. G. Arnaut, S. J. Formosinho, *Journal of Photochemistry and Photobiology A: Chemistry* **1993**, *75*, 1-20.
[61] A. Sytnik, M. Kasha, *Proceedings of the National Academy of Sciences of the United States of America* **1994**, *91*, 8627-8630.
[62] N. Jing, J. Deng, L. Yang, K. Zhao, Z. Wang, X. Cheng, Y. Hua, S. Yin, *Journal of Nanoscience and Nanotechnology* **2010**, *10*, 2161-2163.
[63] P. Pacher, A. Lex, S. Eder, G. Trimmel, C. Slugovc, E. J. W. List, E. Zojer, *Sensors and Actuators B: Chemical* **2010**, *145*, 181-184.
[64] D. K. Aswal, S. Lenfant, D. Guerin, J. V. Yakhmi, D. Vuillaume, *Analytica Chimica Acta* **2006**, *568*, 84-108.
[65] A. J. G. Leenaers, D. K. G. de Boer, *X-Ray Spectrometry* **1997**, *26*, 115-121.
[66] L. G. Parratt, *Phys. Rev.* **1954**, *95*, 359.
[67] L. Névot, P. Croce, *Revue de Physique Appliquée* **1980**, *15*, 19.
[68] D. K. Owens, R. C. Wendt, *Journal of Applied Polymer Science* **1969**, *13*, 1741-1747.
[69] P. S. Davids, I. H. Campbell, D. L. Smith, *J. Appl. Phys.* **1997**, *82*, 6319.
[70] F. Amy, C. Chan, A. Kahn, *Organic Electronics* **2005**, *6*, 85-91.
[71] Gaussian 03, Revision C.02, M. J. Frisch, G. W. Trucks, H. B. Schlegel, G. E. Scuseria, M. A. Robb, J. R. Cheeseman, J. A. Montgomery, Jr., T. Vreven, K. N. Kudin, J. C. Burant, J. M. Millam, S. S. Iyengar, J. Tomasi, V. Barone, B. Mennucci, M. Cossi, G. Scalmani, N. Rega, G. A. Petersson, H. Nakatsuji, M. Hada, M. Ehara, K. Toyota, R. Fukuda, J. Hasegawa, M. Ishida, T. Nakajima, Y. Honda, O. Kitao, H. Nakai, M. Klene, X. Li, J. E. Knox, H. P. Hratchian, J. B. Cross, C. Adamo, J. Jaramillo, R. Gomperts, R. E. Stratmann, O. Yazyev, A. J. Austin, R. Cammi, C. Pomelli, J. W. Ochterski, P. Y. Ayala, K. Morokuma, G. A. Voth, P. Salvador, J. J. Dannenberg, V. G. Zakrzewski, S. Dapprich, A. D. Daniels, M. C. Strain, O. Farkas, D. K. Malick, A. D. Rabuck, K. Raghavachari, J. B. Foresman, J. V. Ortiz, Q. Cui, A. G. Baboul, S. Clifford, J. Cioslowski, B. B. Stefanov, G. Liu, A. Liashenko, P. Piskorz, I. Komaromi, R. L. Martin, D. J. Fox, T. Keith, M. A. Al-Laham, C. Y. Peng, A. Nanayakkara, M. Challacombe, P. M. W. Gill, B. Johnson, W. Chen, M. W. Wong, C. Gonzalez, and J. A. Pople, Gaussian, Inc., Wallingford CT, 2004.
[72] A. D. Becke, *J. Chem. Phys.* **1993**, *98*, 5648.

SUPPORTING INFORMATION FOR

Mechanism of Surface Proton Transfer Doping in Pentacene based OTFTs

*Simon J. Ausserlechner[1], Manfred Gruber[2], Reinhold Hetzel[1], Heinz-Georg Flesch[1], Lukas Ladinig[1], Lucas Hauser[3], Michael Buchner,[2] Ferdinand Schürrer,[2] Anja Haase[4], Gregor Trimmel[3], Karin Zojer[2], and Egbert Zojer[1]**

[1] Institute of Solid State Physics,

Graz University of Technology, Petersgasse 16, 8010 Graz, Austria

[2]Institute of Theoretical and Computational Physics, Graz University of Technology

[3]Institute for Chemistry and Technology of Materials,

Graz University of Technology, Streymayrgasse 9, A-8010 Graz, Austria

[4]Institute for Nanostructure Materials and Photonics,

Joanneum Research, Franz-Pichler-Straße 30, A-8160 Weiz, Austria

1. Device fabrication

2. Cleaning process for glass containers used to grow T-SC/SA layers

3. Details on the chosen measurement procedure

4. Additional data for oxide thickness depended transfer curves

5. Details on the x-ray reflectivity measurement

6. Contact angle measurements

7. NH_3 gas exposure (experimental procedure)

8. HCl vapor exposure (experimental procedure)

9. Additional characteristics for the exposure of (Si|SiOx|pentacene|Au) devices first to hydrochloric acid vapor (HCl) and afterwards to ammonia gas (NH_3)

10. Additionally data on TIPS-pentacene devices exposed to HCl vapor or containing T-SC/SA layers (including structural information)

11. Quantum-mechanical simulations

12. Methodology for drift-diffusion based simulations

13. Comparison between measured and calculated transfer characteristics

14. Detailed discussion of the impact of traps on the device characteristics.

As especially the growth of the T-SC/SA layers is impacted severely by the very details of the fabrication process (especially by minute changes of the water concentration during film growth), we considered it appropriate to provide a relatively detailed description of the applied methodologies.

1. Device fabrication (this is a significantly extended version of the description in the main manuscript)**:**

As substrates (serving also as gate electrodes), we used doped silicon wafers with thermally grown oxides with thicknesses d_{ox} = 102.2 nm, d_{ox} = 147.5 nm, d_{ox} = 152.0 nm, and d_{ox} = 245.0 nm pre-cut into 2 cm x 2 cm pieces. Which of the oxides has been used in a certain experiment is specified in the figure captions in the main text.

The waver with d_{ox} = 102.2 nm was boron doped (company: Silchem) and supplied with a plastic coating on the oxide for protection. To remove this plastic coating, we cleaned them in an ultrasonic bath in ultra-pure water for 2 min, cleaned it with a cleaning liquid (Photonic Cleaning Technology, type: First Contact) that was first brushed onto the waver and then left to dry for ca. 15 minutes. The resulting film was then removed by ultrasonic treatment in ultra-pure water produced with a cleaning system (company: Millipore, type: Simplicity 185; and the resulting specific resistance was in the range of MΩcm) for 2 min. Finally we dried the substrates with carbon dioxide gas. The other wavers were phosphorus doped (company: Siegert Consulting) and were delivered without any coating on the oxide.

As a next step, all substrates were cleaned in a CO_2 gas stream and, finally, the oxide surfaces of the substrates were cleaned and activated by an oxygen plasma etching process using a commercial set-up (company: diener electronic, type: Femto). First the plasma etching chamber was evacuated with a scroll pump (company: Varian, type: SH110) to a pressure of 0.2 mbar. In this context it should be mentioned that the use of an oil-free pump (like a scroll pump) is advantageous, as in XPS experiments performed to study the composition of the wafer surface after the plasma etching step, we found fluorine on the SiO_x surface when using a rotary vane pump most likely due to decomposed pump oil. Subsequently, the chamber was flooded with oxygen (company: Air Liquide, type: Alphagaz oxygen) setting the flow-meter to a value of 90% at an (over) pressure of 2.5 bar. Before starting the plasma etching process, we then waited until the pressure inside the chamber silized at 0.3 mbar. The frequency of the

high frequency generator was 40 kHz and we performed the plasma etching at a power of 100 W for 30 s. After the plasma etching process and the water sonication, the substrates were again cleaned with CO_2 gas.

Afterwards, we put them into cleaned glass containers (for a detailed description of the cleaning procedure see below) filled with ultra-pure water, did an ultrasonic treatment for 2 min and left them inside the bottles for about 25 min. This rendered the oxide surfaces of all samples highly hydrophilic lowering the contact angle of H_2O to below 10°, the limit of our contact-angle measurement set-up (vide infra). This is insofar important as (i) before the plasma etching the contact angles of the different wafer batches differed considerably and (ii) the resulting high concentration of –OH groups on the waver surface is beneficial for the docking of silanes when growing the functional monolayers.

Meanwhile, other glass containers (which we had been held at 80°C least over night) to be used for T-SC/SA layer growth were transferred into the glove box while still being hot. Note: We observed increased thicknesses of the T-SC/SA layers when transferring cooled down glass containers, presumably due to the adsorbed water at the inner walls of the containers, as minute amounts of water significantly impact the layer growth. Inside the glove box (H_2O and O_2 concentration < 1 ppm), each of the substrates was put into a separate glass containers that was filled with 10 ml highly dry toluene (water content of about 7 ppm measured with Karl Fischer Titration). To that we added 10 μl of the T-SC/SA solution, which is a 50 vol % mixture of T-SC/SA molecules and toluene (company: ABCR, product number: AB129108,) and let the layer grow for 16 h. After this time, we put the substrates into glass containers with 6 ml fresh highly dry toluene, sealed the containers, transferred them out of the box, sonicated them for 2 min, and rinsed them with fresh toluene (company: Sigma-Aldrich, product number: 34866). This toluene had a water content of about 29 ppm measured with Karl Fischer Titration. Then we dried the samples using CO_2 gas and annealed them for 30 min at about 100 °C at a pressure of about 0.6 mbar. Between the annealing process and pentacene evaporation as well as between pentacene evaporation and gold deposition the substrates were in air and exposed to light for several hours.

The active layer material pentacene (company: tokyo chemical industry, product number: P0030) was vacuum deposited under high-vacuum conditions (base-pressure in the range of 10-6 mbar) typically some days after growing the T-SC/SA layer. The first 5 nm were

deposited at a rate of 0.02 Å/s and the following 30 nm at a rate of 0.1 Å /s, as measured with a quartz microbalance. During pentacene-growth, the substrates were held at a temperature of 60 ° C. Alternatively, TIPS-pentacene films were deposited from a 1 wt % solution of TIPS-pentacene (company: Sigma-Aldrich, product number: 716006-1G) in toluene (company: Sigma-Aldrich, product number: 34866). The films were fabricated by spin coating (company: Chemat Technology, type: KW-4A) in air with the substrate heated to 60°C using an IR lamp (spin parameters set to: 2000 rpm for 18s and 4000 rpm for 20s). The 50 nm thick (measured with a quartz microbalance) gold (company: Oegussa, quality: fine gold plate) source and drain electrodes were produced at a pressure in the range of 10^{-6} mbar in a home-built evaporation set-up operated inside an Ar glove-box. For technical reasons, the manometer had to be located outside the glove box, i.e., close to the turbomolecular pump. Four transistors were fabricated on each substrate.

2. Cleaning process for glass containers used to grow T-SC/SA layers (as mentioned above, the "state" of the glass bottles has a distinct influence on the growth of the T-SC/SA layer)***:***

We always cleaned 19 glass containers (company: Bartelt, product number: 9.072 303) with 32 ml Hellmanex (company: Hellma, product number: 9-307-010-507) in 1.6 l deionized water with an ultrasonic bath for 25 min. Then we emptied the bucket containing the glasses, refilled it with deionized water, emptied every single glass container, cleaned the bucket with deionized water, put the glass containers back into the bucket and filled it with deionized water until the glass containers were covered with water. Now we did the ultrasonic treatment for 7 min and repeated the whole process two times, but without the bucket cleaning step. As a final cleaning step, every glass bottle was rinsed with ultra-pure water and stored in an oven at 80 °C at least overnight. The ultra-pure water was produced with a cleaning system (company: Millipore, type: Simplicity 185) and the resulting specific resistance was in the range of MΩcm.

3. Details on the chosen measurement procedure:

Before measuring the device characteristics, the pentacene layer around the source and drain areas of the four devices located on each substrate is mechanically removed. This reduces the

apparent gate current by up to two orders of magnitude in our common gate devices. To measure the electronic characteristics of the transistors, we used a Keithley 2636A dual source-meter controlled with a home-made software. We started the transfer sweeps at positive gate bias, reduced V_{GS} in steps of -2 V, setting the delay time, which is the time between applying V_{GS} and the measurement of I_D, to 0.1 s. It should, however, be noted that this is not in all cases the actual time between two measurement, because the integration time for every measurement point is set automatically by Keithley firmware to obtain a sufficient signal to noise ratio. Therefore, at very small currents, significantly increased measurement times were applied. V_{GS} was decreased until we reached the most negative reported gate bias (set to a value that did depend on V_{th}). Then V_{GS} was again increased to the highest positive value reported in the figures. The given device parameters were always determined for the sweep from positive to negative V_{GS}. V_{DS} was -2 V for the data reported in Fig. S1 and Fig. S3, and -60 V for the data in Fig. S4. The very low V_{SD} in the first case was chosen to maximize the linear region for data extraction, while in the TIPS-pentacene devices we applied a larger V_{DS} to avoid too small currents. All measurements were performed under ambient light inside a glove box.

4. Additional data for oxide thickness depended transfer curves:

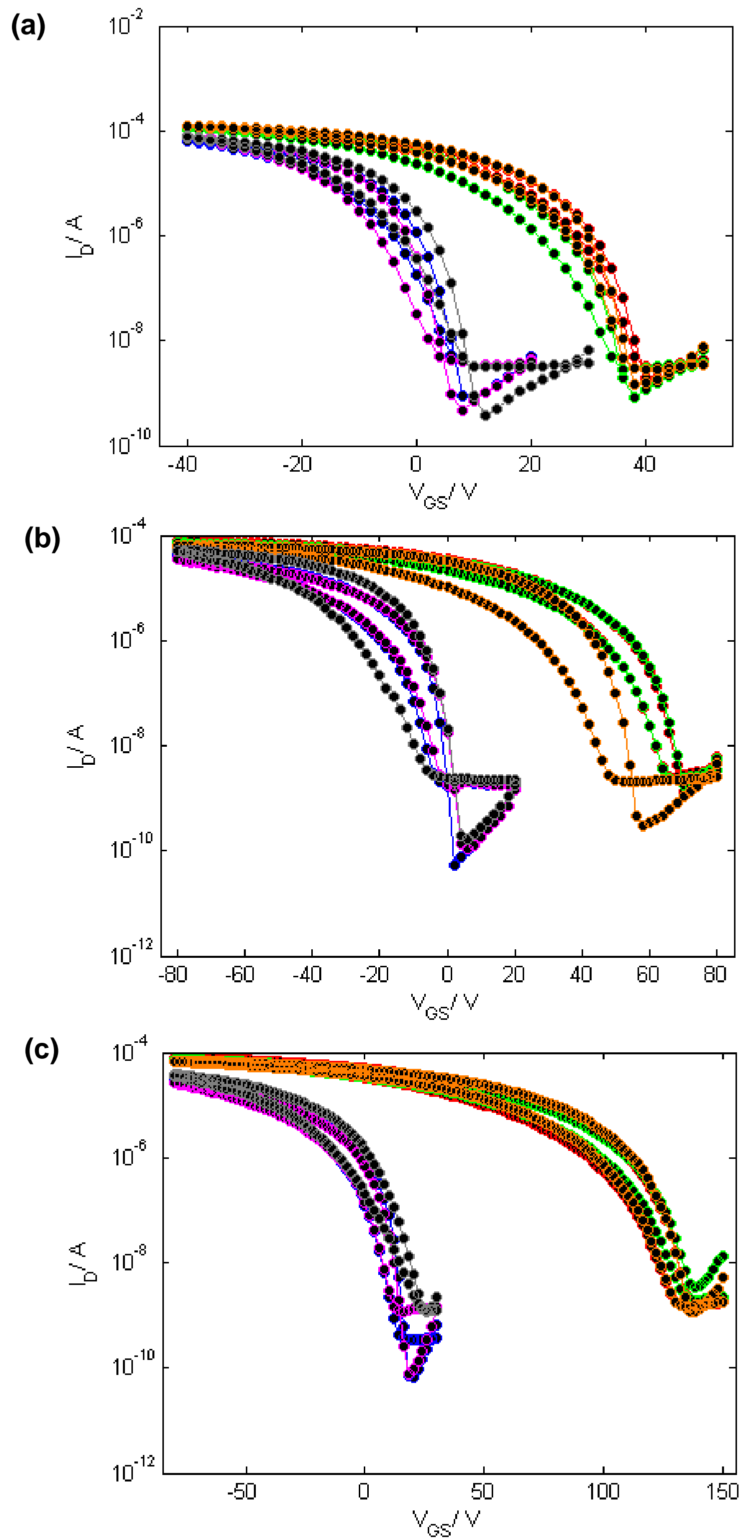

Figure S1: *Additional transfer characteristics of pentacene based devices including a T-SC/SA semiconductor-dielectric interface layer with nominal (actual) oxide thicknesses of* d_{ox-n} *= 100 nm (*d_{ox} *= 102.2 nm),* d_{ox-n} *= 150 nm (* d_{ox} *= 147.5 nm), and* d_{ox-n} *= 250 nm (*d_{ox} *= 245.0 nm). High positive* V_{th} *correspond to devices before and low* V_{th} *to devices after exposure to a flow of pure* NH_3 *gas. The source-drain voltage (*V_{DS}*) was set to -2 V. The*

increased hysteresis in the bottom plot is primarily a consequence of the extended measurement range.

Table S1: *Additional device parameters of (Si|SiOx|T-SC/SA|pentacene|Au) transistors as a function of the oxide thicknesses (d_{ox}) before (top table) and after NH_3 exposure (bottom table). Threshold/onset voltages have been derived with different methods and are denoted as, V_{ELR}, V_{SD}, and V_{SDL} (details see main paper), mobilities (μ), and on to off ratios (I_{on}/I_{off}) are reported. I_{off} is defined as the drain current when the gate voltage equals V_{on} and I_{on} is the current for V_{GS} equaling V_{on} – 40 V. The last line for each oxide thickness gives the average values.*

	c_{ox}	V_{ELR-1} V_{ELR-2} V_{ELR-3}	V_{SD-1} V_{SD-2} V_{SD-3}	V_{SDL-1} V_{SDL-2} V_{SDL-3}	μ_1 μ_2 μ_3	$(I_{on}/I_{off})_1$ $(I_{on}/I_{off})_2$ $(I_{on}/I_{off})_3$
		V_{ELR}	V_{SD}	V_{SDL}	μ	I_{on}/I_{off}
[nm]	[$nFcm^{-2}$]	[V]	[V]	[V]	[$cm^2V^{-1}s^{-1}$]	[10^3]
102.2	34.8	22	29	40	0.22	20
		16	19	36	0.24	30
		22	27	38	0.25	40
		20	25	38	0.24	30
147.5	23.0	40	46	70	0.13	6
		42	46	70	0.11	5
		36	39	56	0.13	50
		39	44	65	0.12	20
245.0	14.1	88	96	136	0.14	2
		85	94	136	0.13	0.8
		96	103	136	0.13	3
		90	98	136	0.13	2

d_{ox}	c_{ox}	$V_{ELR-NH3-1}$ $V_{ELR-NH3-2}$ $V_{ELR-NH3-3}$	$V_{SD-NH3-1}$ $V_{SD-NH3-2}$ $V_{SD-NH3-3}$	$V_{SDL-NH3-1}$ $V_{SDL-NH3-2}$ $V_{SDL-NH3-3}$	μ_{1-NH3} μ_{2-NH3} μ_{3-NH3}	$(I_{on}/I_{off})_{NH3-1}$ $(I_{on}/I_{off})_{NH3-2}$ $(I_{on}/I_{off})_{NH3-3}$
		$V_{ELR-NH3}$	V_{SD-NH3}	$V_{SDL-NH3}$	μ_{NH3}	$(I_{on}/I_{off})_{NH3}$
[nm]	[nFcm^{-2}]	[V]	[V]	[V]	[cm^{2}V^{-1} s^{-1}]	[10^3]
102.2	34.8	-5 -7 -3	0 -1 2	8 6 10	0.20 0.25 0.21	40 70 70
		-5	1	8	0.22	60
147.5	23.0	-17 -14 -17	-11 -9 -7	2 4 4	0.10 0.08 0.14	90 100 80
		-16	-9	3	0.11	90
245.0	14.1	-8 -11 -8	0 -1 -4	18 18 24	0.12 0.10 0.14	70 40 5
		-9	-3	20	0.12	40

5. Details on the x-ray reflectivity measurement:

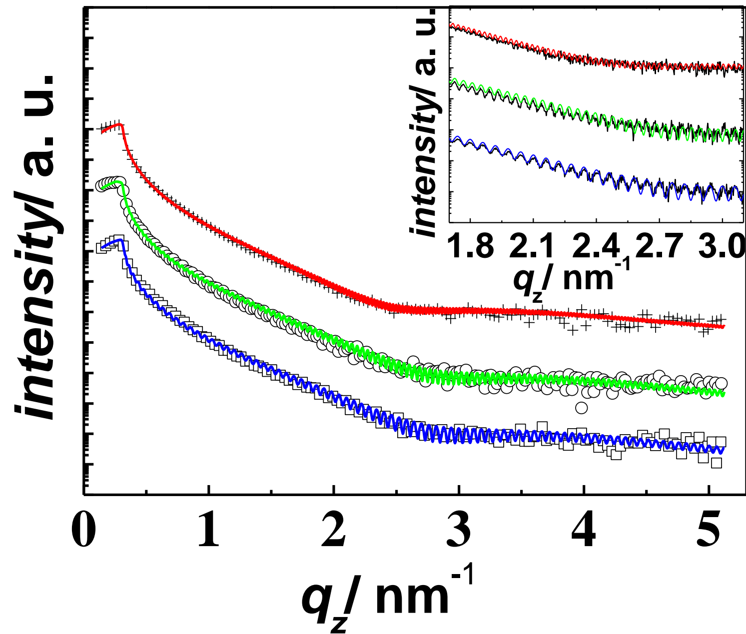

Figure S2. *Specular x-ray reflectivity measurements for three samples with different dox (data points: □: d_{ox} = 102.2 nm, ○: d_{ox} = 147.5 nm, +: d_{ox} = 245.0 nm; and corresponding fit curves). The inset shows a zoom into a smaller q_z range displaying the interference fringes due to the SiO_x layer (curves shifted for clarity).*

The x-ray reflectivity measurements were performed on a Bruker diffractometer (type: D8 Discover) using CuKα-radiation from a sealed tube. For the primary and secondary side optics and the receiving slit a sequence of 0.05mm, 0.1mm and 0.1mm was used. On the secondary side, an automatic absorber is mounted. To analyze the data, we fitted them using WinGixa,[S1] which is an implementation of Parratt's recursive algorithm[S2] including interface, σ_{ox}, and surface root mean square roughness, $\sigma_{T\text{-}SC/SA}$, according to the approach of Nevot and Croce.[S3] The kink around 2.5 nm^{-1} originates from the interference within the T-SC/SA layer, while the fast oscillating fringes (see inset of Fig. S2) are a consequence of interference within the SiO_x layer. To obtain satisfactory agreement between measurements and fits (see Experimental section), the T-SC/SA layers had to be modeled as a double layer structure, i.e. as consisting of two layers with different electron density. The corresponding thicknesses are denoted as $d_{T\text{-}SC/SA\text{-}1}$ and $d_{T\text{-}SC/SA\text{-}2}$. Thus, in total a three-layer structure has been used as a model to fit the experimental data.

6. Contact angle measurements:

The contact angles were measured with a drop shape analysis system (company: Kruess GmbH, type: DSA 100) using deionized water and diiodomethane (company: Sigma-Aldrich, product number: 158429) as test liquids (drop volume ~3 µl). Based on the method by Owens Wendt,[S4] the surface free energy per unit area E_s of the T-SC/SA layers were calculated automatically. The contact angles were obtained by means of the sessile drop method and were measured within 2 seconds.

Table S2: *Diiodomethane Θ_d and water Θ_w contact angles for two independent series for T-SC/SA layers grown on substrates with three different oxide layer thickness d_{ox} and the out of that calculated surface free energy E_s. The σ values are the standard deviations to the corresponding values derived from five independent measurements*

d_{ox}	Θ_{d1} Θ_{d2}	σ_{d1} σ_{d1}	Θ_{w1} Θ_{w2}	σ_{w1} σ_{w2}	E_{s1} E_{s2}	σ_{s1} σ_{s2}
	Θ_d	σ_d	Θ_w	σ_w	E_s	
[nm]	[°]	[°]	[°]	[°]	[mJ*m^{-2}]	[mJ*m^{-2}]
102.2	36.1 34.8	1.0 0.7	66.2 57.7	0.6 1.1	50.2 55.0	0.3 0.3
	35.5		62.0		52.6	
147.5	37.2 35.6	1.1 0.3	68.6 63.1	0.8 0.9	48.7 51.9	0.3 0.1
	36.4		65.9		50.3	
245.0	36.5 38.1	0.81 0.72	70.2 62.1	0.2 1.5	48.2 51.6	0.2 0.3
	37.3		66.2		49.9	

7. NH_3 gas exposure* (experimental procedure)*:

We put our devices in a homemade measurement cell and flooded the cell with NH_3 gas (company: Linde Gas, product number: UN1005), for either 30 min (data in Fig. S1) or 1 min (data in Fig. S3).The NH_3 pressure was 1.5 bar and the volume flow was approximately 8 lh^{-1}. After the NH3 exposure, we flooded the cell with argon gas (company: Air Liquide, type: ALPHAGAZ ARGON 1) until we could not detect ammonia at the gas outlet of the measurement cell. *Hazard warning! NH_3 is highly toxic, thus experiments should always be performed in a fume hood using appropriate gloves and protective glasses!*

8. HCl vapor exposure* (experimental procedure)*:

We put the ready-made devices over a beaker filled with fuming hydrochloric acid (company: Sigma-Adrich, product number: 30721) for 1 min. Hazard warning! *HCl vapor is very acidic thus experiments should always be performed in a fume hood using appropriate gloves and protective glasses!*

9. Additional characteristics for the exposure of (Si|SiOx|pentacene|Au) devices first to hydrochloric acid vapor (HCl) and afterwards to ammonia gas (NH_3):

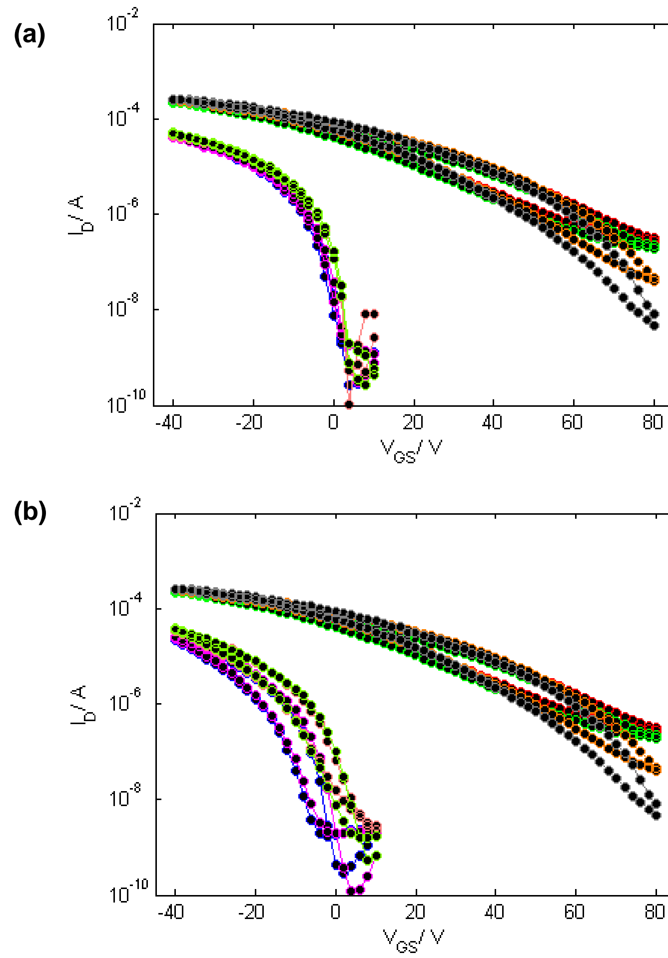

Figure S3: *(a) Transfer characteristics of different devices before (low V_{th}) and after exposure to HCl vapor (high V_{th}); (b) transfer characteristics of the same devices after HCl exposure (high V_{th}) and after subsequently NH_3 (low V_{th}) exposure in the bottom (Fig. 6 (b)).*

10. Additional data on TIPS-pentacene devices exposed to HCl vapor or containing T-SC/SA layers:

TIPS-pentacene devices containing a T-SC/SA layer at the interface between the organic semiconductor and the SiOx dielectric, as well as "conventional" TIPS-pentacene devices exposed to HCl vapor show clearly negative V_{th} and V_{on} in contrast to pentacene based devices (see Fig. S1 and Fig. S3).

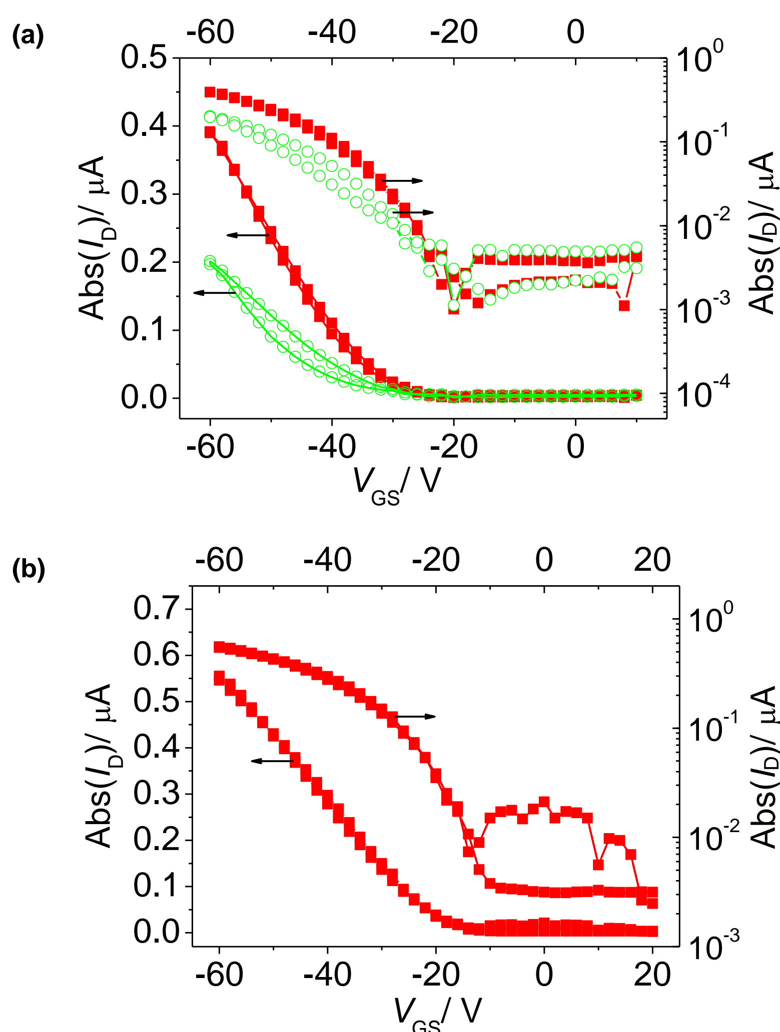

Figure S4: *(a) Transfer characteristic of a (Si/SiOx/TIPS-pentacene/T-SC/SA/Au) device with* d_{ox} *= 152 nm before (solid squares) and after exposure to HCl vapor (open circles). (b) Transfer characteristic of a (Si/SiOx/T-SC/SA/TIPS-pentacene/Au) devices with* d_{ox} *= 152 nm.* V_{DS} *is set to -60 V.*

In this context, it should be mentioned that the investigated TIPS-pentacene films are preferentially aligned in the (001) and (011) orientation as can be inferred from the thin-film x-ray diffraction data shown in Fig. S5. This means that the molecular backbones lie essentially parallel to the substrate surface ((001) orientation) or are somewhat inclined (011 orientation), which is clearly different from the preferential orientation of pentacene on SiO_x, where the molecules typically stand (close to) upright.[S5] This can cause differences in the diffusion of gasses like HCl through the active layer. Considering, however, (i) that no acid doping is observed also for acidic SAMs directly in the channel region, (ii) that the active regions are very thin, which should allow HCl to diffuse right to the channel independent of crystallite orientation and (iii) that there should be a massive impact on the transistor characteristics also if only the regions of the OSC layer close to the surface were doped and thus made conducting, it appears safe to conclude that TIPS-pentacene is not prone to acid doping (at least not when using HCl or T-SC/SA as the reagents)

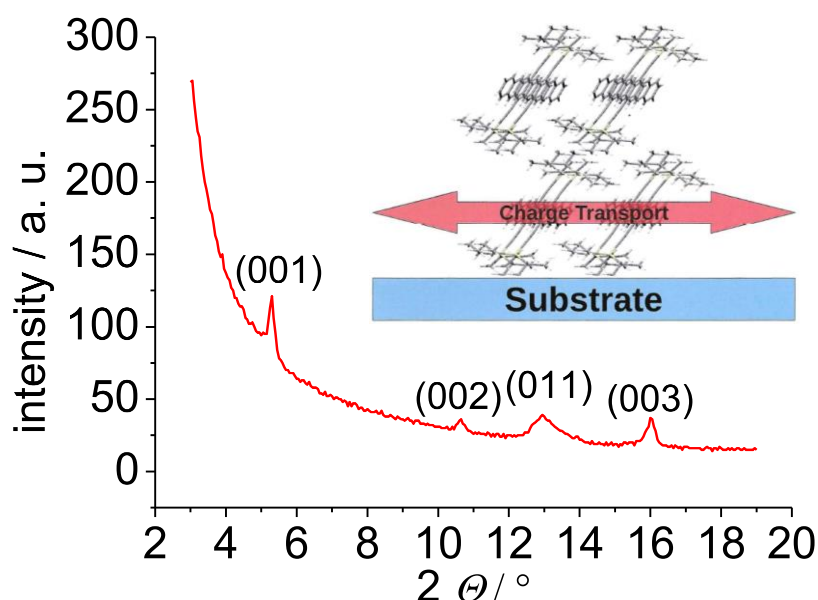

Figure S5: Θ/2Θ scan of a pentacene layer spin-coated from toluene with the substrate held at 60°C. The inset (courtesy of Armin Moser) shows the schematic structure for the (001) orientation.

11 Quantum-mechanical simulations:

The quantum-mechanical calculations were performed using Gaussian03[S6] applying the B3LYP[S7] hybrid functional and a 6-31G(d,p) basis set. Total energies were extracted from the last step in the geometry optimizations. Note that we encountered serious convergence

problems, when optimizing the geometry of planarized TIPS-pentacene protonated at one of the central C-atoms. To circumvent these problems, we first performed a geometry optimization with loose convergence criteria (which did converge), then increased the convergence criteria to the standard values and reduced the step-size in the optimization process. Even this procedure yielded only partially converged geometries (i.e., not all of the geometry convergence criteria could be met). This problem prevailed when changing the optimizer to the Newton algorithm. As the differences between all obtained total energies (fully converged with loose convergence criteria, and partially converged with standard criteria) were smaller than 1 meV, they were eventually accepted as the appropriate values for planarized TIPS-pentacene protonated at one of the central C-atoms. GaussView 2.1[S8] was used to plot the molecular structure in Fig. S6.

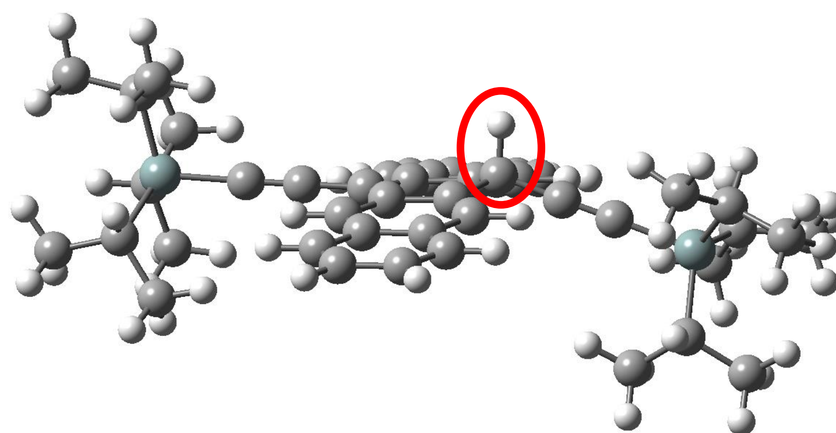

Figure S6. *(a) B3LYP/6-31G(d,p) optimized gas-phase geometry of TIPS-pentacene protonated at the central position.*

Calculations of the reaction enthalpies of proton transfer between T-SC/SA or HCL and pentacene:

Calculations on isolated protonated/deprotonated pentacene, HCL, and TSA molecules yield energy differences between 4.0 eV and 4.7 eV (not correcting for basis-set superposition errors). These energies, however, severely overestimate the actual situation, as they do not consider the Coulomb attraction between the proton and the acid residue and also neglect medium polarization effects, which additionally significantly stabilize the charge-separated situation. Describing the actual situation in the bulk is, however, clearly beyond the scope of the present manuscript and is severely complicated by the unknown details of the interface structure and by DFT's tendency to overestimating charge delocalization.

12. Methodology for drift-diffusion based simulations (this is a significantly extended version of the description in the main manuscript)***:***

The numerical model to describe device characteristics is a two-dimensional drift-diffusion approach as described in Ref. [S9] with special boundary conditions at the source and drain electrodes. Charge carrier injection occurs via thermionic emission and tunneling through a potential barrier (given by the image charge model) in WKB approximation and is corrected by an interface recombination current.[S10] The corresponding system of equations containing the Poisson equation, the drift-diffusion current density equation, and the continuity equation with appropriate boundary conditions is solved self-consistently on a non-regular two-dimensional grid[S9] using an implicit time integration.

During the simulation, the device geometry, the hole injection barrier of 0.47eV from gold into pentacene,[S11] and the dielectric constants of pentacene ($\varepsilon = 3.4$) and SiO_2 ($\varepsilon = 3.9$) are kept fixed. To describe the different onset voltages at different device thicknesses, a fixed negative interface charge distribution with a density of $1.5\text{x}10^{17}$ em^{-2} and an interface dipole layer with a density resulting in a potential shift of 31 V were placed at the pentacene-SiO_x interface. The latter were realized by placing two oppositely charged space charge layers with an areal charge density of 2.0 x 10^{19} em^{-2} at a distance of 3 Å,

To further account for the shape of the I-V curves obtained in the experiments two types of traps are considered: (i) The occurrence of a hysteresis (cf. Fig. S6) is simulated by including bulk traps. The density $p_{trap}(x,y)$ of trapped holes is self-consistently determined for each time step using the rate equation $dp_{trap}(x,y)/dt = 1/\tau'_{trap}\ p(x,y) - 1/\ \tau'_{detrap}\ p_{trap}(x,y)$, where $p(x,y)$ denotes the hole density and τ'_{trap} and τ'_{detrap} are the trapping and detrapping time constants, respectively. The latter are of the order of seconds; the used numerical values are listed in Table S3. For the bulk traps we assume that the available number of trapping sites far exceeds the number of trapped carriers for the considered time scales (i.e., it does not need to be considered explicitly) (ii) To properly account for the shape of the transfer-characteristics in the sub-threshold region (cf. Fig. S6), additional interface traps are incorporated.[S12] To prevent a possible influence on the hysteresis, they are treated as being always in the steady state, which is a reasonable assumption as long as the associated time constants are clearly shorter than the acquisition times for each measurement point. A simulation including a single

trap level is not sufficient to capture the shape of the transfer characteristic at gate voltages close to the threshold-voltage (see next section). This deficiency can be mended by assuming a trap distribution rather than a single trap level. The actual density of trapped carriers p_t is self-consistently determined depending on the mobile carrier density at the interface and the width of the trap distribution. For the sake of simplicity, the trap distribution is assumed to be rectangular shaped, to have a width $\sigma = 0.1$ eV, and to be shifted by $A = 0.1$ eV with respect to the hole transport level E_{HOMO}. I.e., the trap density can be written as $D_t(E)=p_{t0}/\sigma\ \Theta(E-(E_{HOMO}+A))\ \Theta(E_{HOMO}+A+\sigma-E)$ with $\Theta(E')$ denoting the Heaviside function and p_{t0} the total number of traps. To describe the density of trapped carriers, p_t, we solve the following differential equation: $dp_t(x,y)/dt = 1/\tau_{trap}\ (p_{t0}-p_t)/p_{t0}\ p(x,y) - 1/\ \tau_{detrap}\ p_t(x,y)$, where the term $(p_{t0}-p_t)/p_{t0}$ is introduced to provide an upper limit of the total number of trapped carriers; in the steady state one only needs to know the ratio $\tau_{detrap}/\ \tau_{trap}$. For the above described rectangular density of states, the latter becomes: $\tau_{detrap}/\ \tau_{trap} = \exp[(\sigma(1-p_t/p_{t0}) + A)q/k_BT]$, where k_B is the Boltzmann constant, and $T = 298$ K the temperature. The above two equations are solved self-consistently.

Table S3: *Parameters used to simulate the transfer characteristics for all oxide thicknesses d_{ox}. Mobility, μ; acquisition time per data point, t; trapping time constant, τ'_{trap}, and detrapping time constant, τ'_{detrap}, of the long-lived bulk traps; density of the short-lived interface traps, p_{t0}. The values of the hole mobility and the density of interface traps of the 100nm device differ somewhat from the corresponding value in thicker devices. The differently pretreated substrate in the 100 nm device presumably has interface properties that deviate from the 150 nm and 250 nm devices and, thus, alter interface-determined quantities such as mobility and interface trap density. The deviation between the intrinsic mobility used here and the effective mobility extracted from the experiments will be discussed in section 14.*

d_{ox} /nm	μ / cm^2/Vs	t / s	p_{t0} / m^{-2}	τ'_{trap} /s	τ'_{detrap} /s
100	0.34	0.1	3.2x10^{16}	11	4
150	0.21	0.1	4.3x10^{16}	11	4
250	0.23	0.1	4.3x10^{16}	11	4

13. Comparison between measured and calculated transfer characteristics

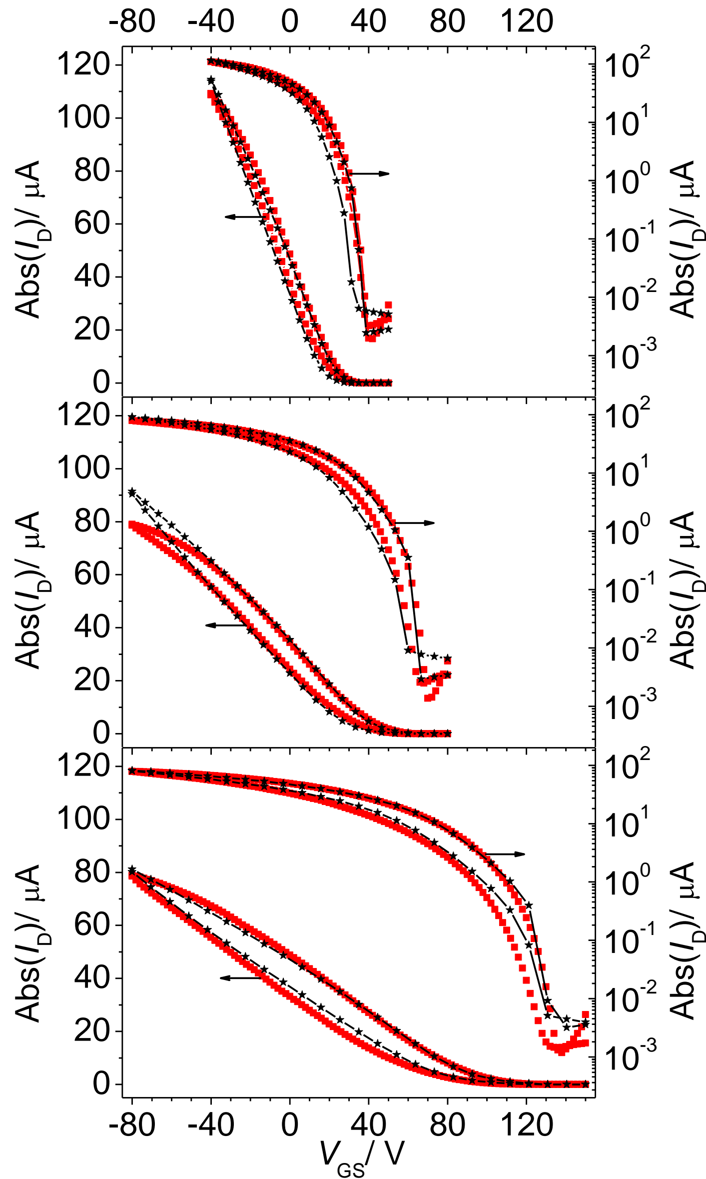

Figure S7. *Comparison between simulated (black stars) and measured (red squares) transfer characteristics (from top to bottom: $d_{ox\text{-}n}$ = 100 nm, $d_{ox\text{-}n}$ = 150 nm and $d_{ox\text{-}n}$ = 250 nm).*

The simulated curves are in an excellent agreement with the measured ones (cf., Fig. S7), in particular, considering that only a few degrees of freedom have been taken to account in the simulations. Reasons for the residual mismatch between theory and experiment could possibly be (i) more sophisticated trap-distributions, (ii) the varying data acquisition time of the Keithley source meter at low device currents (vide supra, resulting in an overestimation of the hysteresis at small currents), and (iii) mobility degradation that affects the high current region. The latter gives rise to an overestimation of I_{DS} for large negative V_{GS}, which could either be

accounted for by a V_{GS}-dependent mobility or assuming a mobility that decreases close to the interface,[S13] where charge carriers are more strongly accumulated at large negative V_{GS}.

14. Detailed discussion of the impact of traps on the device characteristics.

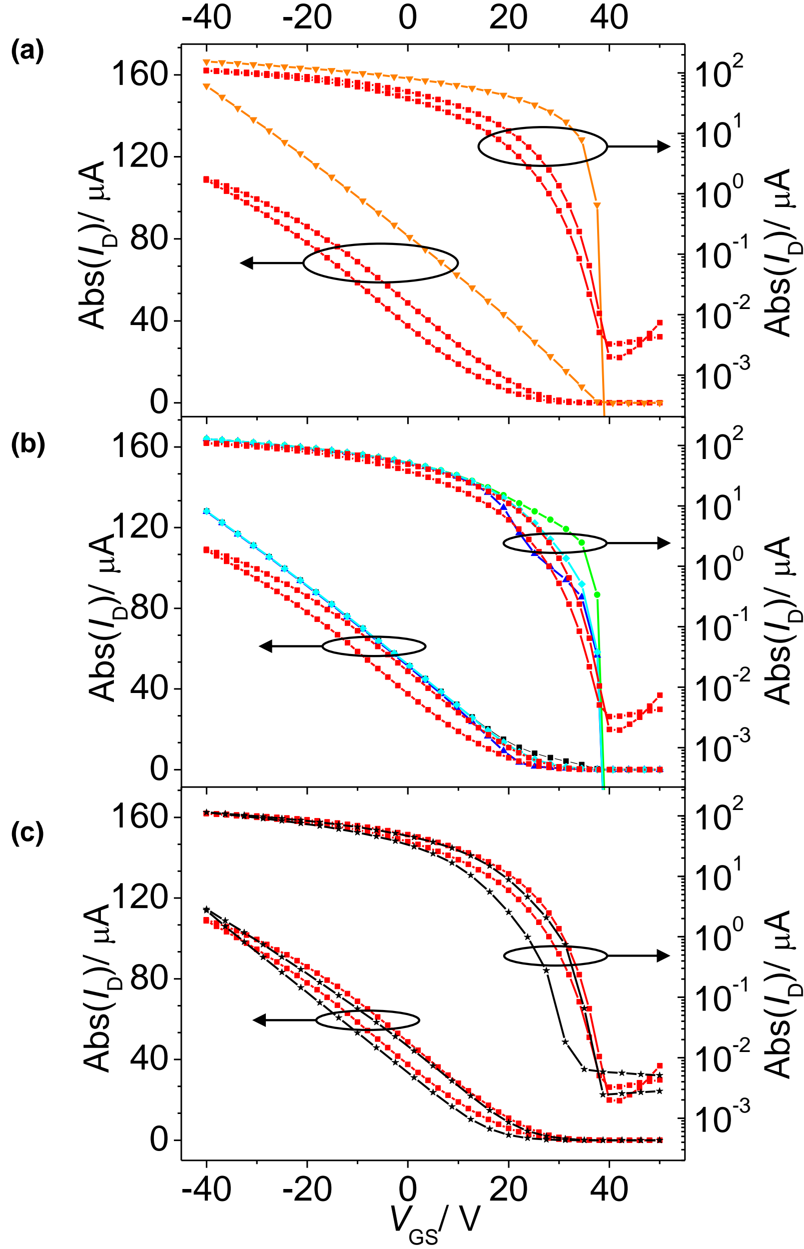

Figure S8. *Linear (left) and semi-logarithmic (right) plot of simulated transfer curves for the d_{ox} = 100 nm device assuming fixed intrinsic mobilities and interface charge layers upon increasing the number of considered effects. The experimental curves are shown as red solid squares for comparison. (a) considering no further effects; (b) comparison between interface trap distributions: a single interface trap level at 0.1 (green solid circles) and 0.2 eV (blue solid triangles) above the transport level and a constant interface trap density between 0.1 eV and 0.2 eV above the hole transport level (cyan solid diamond). (c) "final" model including*

the rectangular interface trap density from b) and bulk traps as described in section 12 black solid stars().

While the general observation of a gate-oxide thickness dependent V_{th} can be consistently modeled by the space charge and dipole densities as discussed extensively in the main manuscript, the detailed shapes of the transfer characteristics are not reproduced in a "straightforward" calculation assuming a fixed carrier mobility and disregarding traps. This becomes obvious from a comparison between Fig. S7 and Fig. S8 (a). To further illustrate that, Figure 7 shows the evolution of the transfer-characteristics upon including an increasing amount of effects. As discussed in the main text, the switch-on voltage is quantitatively captured by the charge distributions at the dielectric-pentacene interface.

Including various types of traps, the full characteristics can, however, be recovered even regarding the hysteresis and a suitable off-current. Which details of the characteristics are affected by which physical effect can be seen in Fig. S8, where we successively increase the complexity of the applied model. Fig. S8 (a) compares the experimental transfer characteristics with the one obtained in the simulations assuming a constant mobility of μ = 0.34 cm^2/Vs. The latter is somewhat larger than that extracted from the experimental data. It can be regarded as an "intrinsic" mobility that is determined by the transport properties of pentacene and by shallow traps that are filled/emptied at time-scales much faster than those relevant for the experiment. It is necessary to start with such a large value of μ, as the "effective" mobility will be reduced when introducing traps in the following steps. A satisfactory agreement between theory and experiment is also not achieved, when using the experimentally determined effective mobility.

The correct description of the shape of the curves (in particular the sub-threshold swing) requires the incorporation of interface traps.[S11] It is important to note here the quality of agreement needs to be assessed both from the linear as well as from the semi-logarithmic plot. As illustrated in Fig S8 (b), the inclusion of a single level of short-lived traps causes the desired reduced slope of the I-V curve in the sub threshold region (circles and triangles). Upon inspecting the curves in the logarithmic plot (corresponding right panel) it , however, becomes evident that a single trap level is even qualitatively not sufficient to reproduce the measurements due to a marked kink, e.g., at V_{GS}=30V for a 0.1 eV trap. Rather, as shown as diamonds in Fig. S8 (b), a distribution of traps can reproduce the shape satisfactorily, since

the resulting “superposition” of trap levels smears out the kinks associated with a single trapping energy. Finally, the incorporation of additional, long-lived traps gives rise to a hysteresis (Fig. S8c). Regarding the origin of residual deviations between theory and experiment see the discussion at the end of section 13.

[S1] A. J. G. Leenaers, D. K. G. de Boer, *X-Ray Spectrometry* **1997**, *26*, 115-121.

[S2] L. G. Parratt, *Phys. Rev.* **1954**, *95*, 359.

[S3] L. Névot, P. Croce, *Revue de Physique Appliquée* **1980**, *15*, 19.

[S4] D. K. Owens, R. C. Wendt, *Journal of Applied Polymer Science* **1969**, *13*, 1741-1747.

[S5] T. Schwieger, X. Liu, D. Olligs, M. Knupfer, Th. Schmidt, Journal of Applied Physics **2004**, 96, 5596.

[S6] Gaussian 03, Revision C.02, M. J. Frisch, G. W. Trucks, H. B. Schlegel, G. E. Scuseria, M. A. Robb, J. R. Cheeseman, J. A. Montgomery, Jr., T. Vreven, K. N. Kudin, J. C. Burant, J. M. Millam, S. S. Iyengar, J. Tomasi, V. Barone, B. Mennucci, M. Cossi, G. Scalmani, N. Rega, G. A. Petersson, H. Nakatsuji, M. Hada, M. Ehara, K. Toyota, R. Fukuda, J. Hasegawa, M. Ishida, T. Nakajima, Y. Honda, O. Kitao, H. Nakai, M. Klene, X. Li, J. E. Knox, H. P. Hratchian, J. B. Cross, C. Adamo, J. Jaramillo, R. Gomperts, R. E. Stratmann, O. Yazyev, A. J. Austin, R. Cammi, C. Pomelli, J. W. Ochterski, P. Y. Ayala, K. Morokuma, G. A. Voth, P. Salvador, J. J. Dannenberg, V. G. Zakrzewski, S. Dapprich, A. D. Daniels, M. C. Strain, O. Farkas, D. K. Malick, A. D. Rabuck, K. Raghavachari, J. B. Foresman, J. V. Ortiz, Q. Cui, A. G. Baboul, S. Clifford, J. Cioslowski, B. B. Stefanov, G. Liu, A. Liashenko, P. Piskorz, I. Komaromi, R. L. Martin, D. J. Fox, T. Keith, M. A. Al-Laham, C. Y. Peng, A. Nanayakkara, M. Challacombe, P. M. W. Gill, B. Johnson, W. Chen, M. W. Wong, C. Gonzalez, and J. A. Pople, Gaussian, Inc., Wallingford CT, 2004.

[S7] A. D. Becke, *J. Chem. Phys.* **1993**, *98*, 5648.

[S8] Gauss View 2.1, Gaussian Inc. Pittsburgh USA, **2000**.

[S9] S. K. Possanner, K. Zojer, P. Pacher, E. Zojer, F. Schürrer, *Adv. Funct. Mater.* **2009**, *19*, 958-967.

[S10] P. S. Davids, I. H. Campbell, D. L. Smith, *J. Appl. Phys.* **1997**, *82*, 6319.

[S11] F. Amy, C. Chan, A. Kahn, *Organic Electronics* **2005**, *6*, 85-91.

[S12] S. Scheinert, G. Paasch, M. Schrödner, H.-K. Roth, S. Sensfuß, T. Doll, *J. Appl. Phys.* **2002**, *92*, 330.

[S13] M. Mottaghi, G. Horowitz, *Organic Electronics* **2006**, *7*, 528-536.